Transcription factor control of dendrite targeting via combinatorial cell-surface codes

Qijing Xie[1,2,6], Jiefu Li[1,6], Hongjie Li[1,5], Namrata D. Udeshi[3], Tanya Svinkina[3], Sayeh Kohani[1], Ricardo Guajardo[1], D.R. Mani[3], Chuanyun Xu[1], Tongchao Li[1], Shuo Han[4], Wei Wei[1], S. Andrew Shuster[1,2], David J. Luginbuhl[1], Alice Y. Ting[4], Steven A. Carr[3] & Liqun Luo[1,*]

[1]Department of Biology, Howard Hughes Medical Institute, Stanford University, Stanford, CA 94305, USA
[2]Neurosciences Graduate Program, Stanford University, CA 94305, USA
[3]The Broad Institute of MIT and Harvard, Cambridge, MA 02142, USA
[4]Departments of Genetics, Biology, and Chemistry, Chan Zuckerberg Biohub, Stanford University, Stanford, CA 94305, USA
[5]Present Address: Huffington Center on Aging, Department of Molecular and Human Genetics, Baylor College of Medicine, Houston, TX 77030, USA
[6]These authors contributed equally: Qijing Xie, Jiefu Li
[*]Correspondence: lluo@stanford.edu (L.L.)

Abstract

Transcription factors are central commanders specifying cell fate, morphology, and physiology while cell-surface proteins execute these commands through interaction with cellular environment. In developing neurons, it is presumed that transcription factors control wiring specificity through regulation of cell-surface protein expression. However, the number and identity of cell-surface protein(s) a transcription factor regulates remain largely unclear[1,2]. Also unknown is whether a transcription factor regulates the same or different cell-surface proteins in different neuron types to specify their connectivity. Here we use a lineage-defining transcription factor, Acj6 (ref. [3]), to investigate how it controls precise dendrite targeting of *Drosophila* olfactory projection neurons (PNs). Quantitative cell-surface proteomic profiling of wild-type and *acj6* mutant PNs in intact developing brains and a proteome-informed genetic screen identified PN surface proteins that execute Acj6-regulated wiring decisions. These include canonical cell adhesion proteins and proteins previously not associated with wiring, such as the mechanosensitive ion channel Piezo—whose channel activity is dispensable for its wiring function. Comprehensive genetic analyses revealed that Acj6 employs unique sets of cell-surface proteins in different PN types for dendrite targeting. Combinatorial expression of Acj6 wiring executors rescued *acj6* mutant phenotypes with higher efficacy and breadth than expression of individual executors. Thus, a key transcription factor controls wiring specificity of different neuron types by specifying distinct combinatorial expression of cell-surface executors.

Most instructive molecules for neuronal wiring discovered thus far fall into two categories—transcription factors and cell-surface proteins[1,2,4-6]. Transcription factors determine the fate of a neuron including its connectivity, whereas cell-surface proteins instruct neurites to navigate through complex environments and establish connection specificity. We systematically studied how a transcription factor controls dendrite targeting specificity by regulating cell-surface protein expression.

Acj6 shapes the PN surface proteomic milieu

Acj6 is a member of POU domain transcription factors, which are widely used from *C. elegans* to mammals to regulate neural development[3,7-9]. In the fly olfactory system, about 50 types of cholinergic excitatory projection neurons (PNs) are derived from two distinct neuroblast lineages[10]. Each PN type targets dendrites to a stereotyped antennal lobe glomerulus according to its lineage and birth order[10-13]. Acj6 is specifically expressed in postmitotic neurons in the anterodorsal PN (adPN) lineage, but not the lateral PN (lPN) lineage (**Fig. 1a**), to instruct the precise dendrite targeting of adPNs[3].

Acj6 may regulate dendrite targeting through direct transcriptional regulation of cell-surface proteins or through intermediate transcription factors and post-transcriptional mechanisms. To capture the entirety of Acj6-regulated cell-surface proteins, we performed PN-surface proteomic profiling in intact wild-type or *acj6* mutant fly brains (**Fig. 1b**) at 36–40 hours after puparium formation (APF), when PN dendrites are actively making wiring decisions. Briefly, membrane-tethered horseradish peroxidases (HRP) expressed on PNs convert the membrane-impermeable biotin-xx-phenol (BxxP) substrate to phenoxyl radicals in the presence of H_2O_2[14], which promiscuously biotinylate proteins on the PN surface[15]. This approach led to biotinylation of PN-surface proteins with high spatial specificity (**Extended Data Fig. 1a**).

We applied an 8-plex tandem mass tag (TMT)-based quantitative mass spectrometry strategy to identify those biotinylated proteins[15,16] (**Fig. 1c**). For each genotype, in addition to two biological replicates, we also included two negative controls, in which either H_2O_2 or HRP was omitted to account for non-specific bead binders, endogenously biotinylated proteins, and labeling by endogenous peroxidases. Each sample (derived from ~1100 dissected pupal brains) was separately lysed and enriched with streptavidin beads (**Extended Data Fig. 1b**). After on-bead trypsin digestion and TMT labeling, all samples were pooled for mass spectrometry analysis.

Biological replicates in both genotypes showed high correlation (**Extended Data Fig. 1c**), illustrating the robustness of our method. Additionally, loss of Acj6 did not cause global disruption of transcription (**Extended Data Fig. 1d).** We ranked proteins by their experimental-to-control TMT ratios in a descending order and found that known plasma membrane proteins were enriched while contaminants were sparse at the top of those ranked lists (bottom left corner, **Fig. 1d**). Therefore, we filtered out contaminants using experimental-to-control TMT ratios[15,17] (**Fig. 1e** and **Extended Data Fig. 1e**), yielding PN surface proteomes of 459 and 537 proteins for wild-type and *acj6* mutant, respectively (**Extended Data Fig. 1f**). Cellular Component terms classified by Gene Ontology analysis showed that both proteomes consisted of proteins localized at the cell surface, confirming the spatial specificity of our approach (**Fig. 1f**, top). Top Biological Process terms showed enrichment of neural developmental processes in both proteomes (**Fig. 1f**, bottom), matching the developmental stage at which we conducted PN surface profiling.

Many proteins exhibited altered expression on the *acj6* mutant PN surface (**Fig. 1g**). These include proteins belonging to classic adhesion protein families—Off-track (Otk), Sidestep-V (Side-V), and Dprs in the immunoglobulin (Ig) superfamily, and Reduced ocelli (Rdo) and Tartan (Trn) in the leucine-rich repeat superfamily. We also observed several proteins known to participate in neuronal function—the mechanosensitive ion channel Piezo, the dopamine receptors Dop1R1 and Dop2R, and the voltage-gated sodium channel subunit α_1 Cacophony (Cac). Most of these proteins were also identified using a more stringent cutoff criterion (**Extended Data Fig. 2**).

A proteome-informed genetic screen

Among the Acj6-regulated PN surface proteins we identified, Trn was the only one known to participate in PN dendrite targeting[18]. Therefore, we performed genetic screens to systematically identify Acj6 targets with wiring functions by knocking down (with *UAS-RNAi*) or overexpressing (with *UAS-cDNA*) candidates whose expressions were down- or up-regulated on the *acj6* mutant PN surface, respectively, using a split *adPN-GAL4* (Methods). Due to the limited availability of existing *UAS-cDNA* lines for overexpression, most candidates we tested were downregulated in *acj6* mutant, which means that Acj6 normally promotes their expression.

We scored the innervation extent of 38 glomeruli in each antennal lobe for each genotype (**Extended Data Fig. 3a**, **4**). To determine whether altering the expression of these Acj6-regulated PN surface proteins caused significant dendrite targeting changes, the innervation extent of each glomerulus in each genotype was compared to control using a Chi-squared test (**Extended Data Fig. 3**). We identified many new molecules required for PN dendrite targeting (**Fig. 2a**). These include Otk, Neprilysin 3 (Nep3), and Dystroglycan (Dg), which have been previously shown to be required for neurite targeting of other neuron types[15,19-21]. In addition, knockdown of *Dop1R1*, *Dop2R, stolid* (*stol*), and *Piezo*, which are traditionally thought to mediate neuronal function instead of development, also caused PN wiring defects. Previously uncharacterized genes, such as *CG5027*, also contributed to the targeting accuracy of PN dendrites.

As with knocking down *acj6* itself, knocking down Acj6-regulated cell-surface proteins caused abnormal targeting of adPN dendrites to many glomeruli. Notably, these ectopic targeting or loss of targeting resembled *acj6-RNAi* in multiple glomeruli including DA4m, DA4l, VA7l, VA3, and DM4 (**Fig. 2a**). Furthermore, dendrite targeting to an individual glomerulus can be affected by knocking down several different molecules. These data suggest that many Acj6-regulated cell-surface proteins indeed regulate wiring specificity, and that proper targeting of some PN dendrites requires multiple cell-surface proteins controlled by Acj6.

Otk is a cell-surface wiring executor for Acj6

To establish causal relationships between Acj6 and its targets in regulating wiring specificity, we tested whether expression of specific Acj6-downregulated cell-surface proteins can rescue *acj6* mutant phenotypes (**Fig. 2b**) using mosaic analysis with a repressible cell marker[22] (MARCM; **Extended Data Fig. 5**) with null mutant alleles and full-length cDNA transgenes.

We first investigated Otk, a transmembrane protein containing five extracellular Ig-like domains implicated in axon guidance in embryonic motor axons[19] and photoreceptor axons[20]. We generated a conditional tag to examine endogenous Otk expression specifically in PNs (**Extended Data Fig. 6a–c**). We found that Otk was normally expressed in subsets of both Acj6-positive adPNs and Acj6-negative lPNs during development (**Fig. 2c**). In *acj6* mutant, there was an apparent overall decrease in Otk signal (**Fig. 2d**). Quantification of fluorescence intensity in individual glomeruli revealed that Otk expression was indeed decreased in many adPNs such as DL1 (**Fig. 2d, e**), but not in lPNs such as VA5 (**Fig. 2d** and **Extended Data Fig. 6d**). Thus, Acj6 promotes Otk expression on the surface of a subset of adPNs.

To test if Acj6 regulates Otk expression to instruct adPN dendrite targeting, we focused on single-cell clones of DL1 PNs **(Extended Data Fig. 5b).** In wild-type animals, dendrites of DL1 PNs are confined to a specific glomerulus located in a posterior section of the antennal lobe (**Fig. 2f**, outlined in the bottom panel). Deleting *acj6* or *otk* in DL1 PNs yielded nearly identical mistargeting phenotypes: DL1 PN dendrites mistargeted to both nearby posterior glomeruli as well as the distant DA4m glomerulus in the anterior antennal lobe (**Fig. 2g, h**). Furthermore, both local

and long-range mistargeting phenotypes in *acj6* mutant were partially rescued by expressing *otk* in DL1 single cell clones (**Fig. 2i–k**). This incomplete rescue is consistent with the observation that $otk^{-/-}$ clones had lower phenotypic penetrance than $acj6^{-/-}$ clones (**Fig. 2j, k**) and suggests that Acj6 controls the expression of additional wiring molecule(s) in DL1 PNs to ensure precise dendrite targeting.

These single-cell clone analyses (**Fig. 2f–k)**, together with the observation that Otk expression was decreased in *acj6* mutant DL1 PNs (**Fig. 2e**), demonstrated that Acj6 directs precise targeting of DL1 PN dendrites in part by cell-autonomously promoting Otk expression.

Channel-independent function of Piezo in dendrite targeting

An unexpected observation in our genetic screen was that knocking down the mechanosensitive ion channel, Piezo, disrupted normal PN dendrite targeting (**Fig. 2a** and **Extended Data Fig. 3b**). MARCM analysis using a *piezo* null mutant[23] confirmed that both $acj6^{-/-}$ and $piezo^{-/-}$ adPNs in neuroblast clones mistargeted their dendrites to the DL2 and VL2a glomeruli (**Fig. 3a–c**), albeit with a lower penetrance in $piezo^{-/-}$ PNs (**Fig. 3i, j**). Expressing wild-type *piezo* in adPN neuroblast clones not only rescued *piezo* mutant phenotypes (**Fig. 3e, j**), but also partially rescued *acj6* mutant phenotypes (**Fig. 3d, i**). Thus, Piezo is an executor for Acj6 in controlling dendrite targeting.

Is the ion channel activity of Piezo required for instructing PN dendrite targeting? The atomic structure of mouse Piezo1 showed that amino acids M2493 and F2494 sit on the 'neck' of the pore[24]. These two amino acids are highly conserved from insects to mammals (**Fig. 3f**) Substituting these two amino acids to alanines completely abolishes the ion channel activity of mouse Piezo1 while leaving its trimeric assembly and surface expression intact[24]. We thus generated an equivalent channel-dead version of fly Piezo: $Piezo^{MF\rightarrow AA}$. Unexpectedly, expressing $piezo^{MF\rightarrow AA}$ in adPN neuroblast clones rescued dendrite targeting deficits of *acj6* and *piezo* mutants to the same extent as expressing wild-type *piezo* (**Fig. 3g–j**). We further examined the Acj6-negative lPNs and observed that loss of Piezo also caused dendrite mistargeting, which was rescued by wild-type Piezo or $Piezo^{MF\rightarrow AA}$ (**Extended Data Fig. 7**). This indistinguishable rescuing capacity of wild-type and channel-dead Piezos suggested that Piezo regulates PN dendrite targeting independently of its ion channel activity.

Acj6 employs combinatorial cell-surface codes

In addition to Otk and Piezo, we expressed in $acj6^{-/-}$ adPN neuroblast clones six additional cell-surface proteins that were downregulated in *acj6* mutant and examined dendrite innervation patterns in a broader set of PNs (**Extended Data Fig. 8)**. We assessed whether expression of Acj6-regulated cell-surface proteins improved wiring precision of $acj6^{-/-}$ adPN dendrites by Chi-squared tests comparing the innervation extent of each glomerulus in each rescue experiment to that in control or $acj6^{-/-}$ (**Fig. 4a** and **Extended Data Fig. 9**).

As shown in each row of **Fig. 4a**, expression of seven out of eight cell-surface proteins rescued a subset of $acj6^{-/-}$ phenotypes, including ectopic targeting (red squares in **Fig. 4a**; **Extended Data Fig. 8a–f**) and loss of innervation (blue squares in **Fig. 4a**; **Extended Data Fig. 8g–l**). Specific glomerular mistargeting was rescued by specific cell-surface proteins. For example, loss of VM2 targeting in $acj6^{-/-}$ adPN neuroblast clones was rescued by Piezo, Otk, and Dop2R (**Fig. 4b** and **Extended Data Fig. 8g, h**), while loss of VA1v targeting was rescued by Nep3 (**Extended Data Fig. 8i, j**). This is consistent with our observation that loss of one cell-surface protein resembled only a subset of $acj6^{-/-}$ phenotypes (**Fig. 2a and Extended Data Fig. 3**).

Notably, phenotypic rescues by different cell-surface proteins were largely non-overlapping (**Fig. 4a**), indicating that Acj6 uses distinct cell-surface executors in different PN types for dendrite targeting.

The limited rescue of a small subset of *acj6* mutant phenotypes by each cell-surface protein prompted us to examine whether combinatorial expression could better rescue wiring defects caused by loss of *acj6*. We tested seven combinations of two Acj6-regulated cell-surface proteins and found that these combinations indeed led to overall stronger and broader rescue of $acj6^{-/-}$ wiring defects in adPN neuroblast clones (more white and lighter colored squares in **Fig. 4c** than in **Fig. 4a**). A closer examination of these combinations revealed different modes of genetic interactions between Acj6-regulated cell-surface executors, which collectively contributed to the improved rescuing efficacy.

The most frequently observed interaction mode is additive. The first type of additive interaction was two candidates with partial rescues "summing up" to produce an almost complete rescue when co-expressed. For instance, expression of either Otk or Piezo partially restored innervation to the VM2 glomerulus (**Fig. 4b, d** and 'd' squares in **Fig. 4a**). Co-expression of Otk and Piezo led to wild-type-like innervation in the VM2 glomerulus (**Fig. 4b, d** and the 'd' square in **Fig. 4c**). When Piezo was coupled with Dg, they reduced ectopic targeting to the DL2 glomerulus from ~80% in *acj6* mutant to less than 20% (**Fig. 4e** and 'e' squares in **Fig. 4a, c**). Occasionally, subtractive interaction occurred when one candidate counteracts (**Extended Data Fig. 10**). Whereas the first type of additive interaction above occurred with respect to a specific glomerulus, the second type occurred across glomeruli. For example, Dop2R but not Dg expression rescued loss of innervation to the DA3 glomerulus, while Dg but not Dop2R expression rescued ectopic targeting to the VA6 glomerulus (**Fig. 4a**, black dots). When Dop2R and Dg were co-expressed, both DA3 and VA6 phenotypes were rescued (**Fig. 4c**, black dots).

Besides additive interactions, we also observed synergistic interactions. For example, neither Otk nor Dop1R1 expression alone significantly rescued VL2a ectopic targeting in *acj6* mutant (**Fig. 4f** and 'f' squares in **Fig. 4a**). However, co-expressing both reduced the mistargeting rate from more than 70% in mutant to ~30% (**Fig. 4f** and the 'f' square in **Fig. 4c**), suggesting that both are required for dendrite targeting. In another case, Dop2R expression alone could not significantly rescue DA4m ectopic targeting but, when co-expressed with Otk, it significantly enhanced rescue by Otk (**Fig. 4g** and 'g' squares in **Fig. 4a, c**).

Taken together, these results indicate that Acj6-regulated executors act combinatorically—both between different PN types and within the same PN types—to instruct dendrite targeting, and that different PN types employ distinct cell-surface combinatorial codes for their precise targeting (**Fig. 4h**).

Discussion

For most transcription factors directing neuronal connectivity, their cell-surface wiring executors remain elusive due to the lack of approaches for systematically identifying them. RNA sequencing can determine how deleting a transcription factor alters the transcriptome of developing neurons[25-28], but the transcriptome and proteome of the same cell type often exhibit modest to poor correlations[29-31], particularly for membrane proteins whose trafficking and turnover are subject to extensive post-translational regulation[15,32,33]. In this study, we directly examined the expression of

cell-surface proteins[15,34-37] using *in situ* cell-surface proteomic profiling and systematically identified cell-surface executors for the lineage-specific transcription factor Acj6 in the wiring of fly olfactory PNs.

We identified many Acj6 executors via both loss-of-function and rescue experiments. These include the fly ortholog of the mechanosensitive ion channel Piezos[38,39], which mediate somatosensory and interoceptive mechanotransduction and cell volume regulation[23,40-45]. Piezo also regulates neurodevelopmental processes and axon regeneration[46-48]. However, all known Piezo functions thus far have been attributed to its mechanosensitive ion channel activity. We found that Piezo instructs PN dendrite targeting, and its ion channel activity is dispensable for this function. Future identification of Piezo's extracellular molecular partners may reveal how Piezo instructs dendrite targeting. Besides Piezo, our proteome-informed genetic screen discovered other unconventional wiring molecules for PN dendrite targeting such as the dopamine receptors, highlighting the functional versatility of these molecules in multiple biological contexts. It will be interesting to explore whether these molecules regulate neuronal wiring via their conventional molecular functions or through currently unknown mechanisms like Piezo.

Our systematic examination of Acj6 executors in PN dendrite targeting by RNAi knockdown and rescue experiments revealed that different PN types require different cell-surface proteins for dendrite targeting (columns in **Fig. 4a**), and each molecule often controls a few distinct PN types (rows in **Fig. 4a**). Moreover, combinatorial expression of Acj6 executors yielded stronger and broader rescues of specific *acj6* mutant phenotypes than expressing individual executors (**Fig. 4c**). These data provided *in vivo* evidence for a long-standing hypothesis in developmental neurobiology[49] that neuronal wiring is controlled by a combinatorial code of cell-surface proteins—each neuron type uses a unique combination of wiring proteins, and each protein is used in multiple neuron types (**Fig. 4h**).

Our findings illustrate a divergent 'transcription factor → cell-surface executor' relationship: one transcription factor regulates many cell-surface proteins that execute its function. This could not have been discovered in previous studies when only one or two wiring executors of a transcription factor were examined[1]. On the other hand, Acj6-regulated cell-surface proteins often also have Acj6-independent expression and function (**Fig. 2c** and **Extended Data Fig. 3b, 6d, 6g, 6h, 7**). Thus, they must also be regulated by other transcription factors. Moreover, the presence of Acj6+ PNs that do not express Otk or Dg indicated that Acj6 differentially regulates cell-surface protein expression among different adPN types (**Fig. 2c, 2d** and **Extended Data Fig. 6d, 10b**), demanding the involvement of other transcription factors; otherwise, Acj6 would uniformly regulate each executor in all Acj6+ PN types. Therefore, the 'transcription factor → cell-surface executor' relationship is also convergent: multiple transcription factors regulate the expression of one cell-surface protein. We thus propose the existence of two intertwined combinatorial codes—one of the transcription factors, which specifies the other one of cell-surface executors—to determine neuronal wiring specificity (**Fig. 4i**).

Since transcription factors often serve as central commanders of cellular functions while cell-surface proteins work as direct executors in cell-cell interactions, the 'transcription factor → cell-surface executor → physiological function' framework is of importance for not only neural circuit wiring but also all other biological processes involving cells communicating with their environment. Thus, our approach for systematically identifying cell-surface executors of a transcription factor's function can be applied to address a broad spectrum of biological questions.

Methods

Drosophila stocks and genotypes

Flies were maintained on standard cornmeal medium with a 12 hr light–dark cycle at 25°C, except for the RNAi/overexpression screen in which flies were raised at 29°C. The following lines were used in this study: *tubP-GAL80* and *UAS-mCD8-GFP* (ref.[50]), *hsFlp* (ref.[51]), *FRT19A*, *FRT40A*, and *FRT42D* (ref.[52]), *GH146-Flp* (ref.[18]), *acj6*^{6} (ref.[53]), *otk*^{3} (ref.[19]), *Piezo*^{KO} (ref.[23]), *VT033006-GAL4* (ref.[54]), *GH146-GAL4* (ref.[55]), *C15-p65*^{AD} (ref.[56]), *UAS-HRP-CD2* (ref.[57]), *UAS-dcr2* (ref.[58]), *UAS-otk* (ref.[19]), *UAS-acj6-J* (ref.[59]), *UAS-Dop2R* (ref.[60]), and *UAS-Dg* (Robert Ray, Francis Crick Institute). The RNAi lines were generated previously[58,61,62] and acquired from the Bloomington *Drosophila* Stock Center and the Vienna *Drosophila* Resource Center. *VT033006-GAL4*^{DBD} is an unpublished reagent kindly provided by Yoshi Aso (Janelia Research Campus). *UAS-Piezo*, *UAS-piezo*$^{MF\rightarrow AA}$, *UAS-Dop1R1*, *UAS-Nep3*, *UAS-CG5027*, *UAS-Osty*, *otk-FRT-V5-STOP-FRT-FLAG-STOP*, and *Dg-FRT-V5-STOP-FRT-FLAG-STOP* were generated in this study and are available upon request. Complete genotypes of flies used in each experiment are described in **Supplementary Table 1**.

Biotinylation of PN-surface proteins

PN surface biotinylation was performed following the previously published method[15]. Briefly, we dissected wild-type or *acj6* mutant brains expressing HRP-rCD2 by PNs in pre-chilled Schneider's medium (Thermo Fisher), removed the optic lobes, and transferred them into 500 µL of the Schneider's medium in 1.5 mL protein low-binding tubes (Eppendorf) on ice. Brains were washed with fresh Schneider's medium to remove fat bodies and debris and were incubated in 100 µM of BxxP in Schneider's medium on ice for one hour. Brains were then labeled with 1 mM (0.003%) H_2O_2 (Thermo Fisher) for 5 minutes, and immediately quenched by five thorough washes using quenching buffer (10 mM sodium ascorbate [Spectrum Chemicals], 5 mM Trolox [Sigma-Aldrich], and 10 mM sodium azide [Sigma-Aldrich] in phosphate buffered saline [PBS; Thermo Fisher]). After the washes, the quenching solution was removed, and brains were either fixed for immunostaining (see below for details) or were snapped frozen in liquid nitrogen and stored at –80°C for the proteomic sample collection. For the proteomic sample collection, 1100 dissected and biotinylated brains were collected for each experimental group (8800 brains in total).

Collection of biotinylated proteins

For each proteomic sample, there were five tubes each containing ~220 dissected brains. We added 40 µL of high-SDS RIPA (50mM Tris-HCl [pH 8.0], 150 mM NaCl, 1% sodium dodecyl sulfate [SDS], 0.5% sodium deoxycholate, 1% Triton X-100, 1x protease inhibitor cocktail [Sigma-Aldrich; catalog # P8849], and 1 mM phenylmethylsulfonyl fluoride [PMSF; Sigma-Aldrich]) to each of those tubes, and grinded the samples on ice using disposable pestles with an electric pellet pestle driver. Tubes containing brain lysates of the same experimental group were spun down, merged, and rinsed with an additional 100 µL of high-SDS RIPA to collect remaining proteins. Samples were then vortexed briefly, sonicated twice for ten seconds each, and incubated at 95°C for five minutes to denature postsynaptic density proteins. 1.2 mL of SDS-free RIPA buffer (50 mM Tris-HCl [pH 8.0], 150 mM NaCl, 0.5% sodium deoxycholate, 1% Triton X-100, 1x protease inhibitor cocktail and 1 mM PMSF) were added to each sample, and the mixture was rotated for two hours at 4°C. Lysates were then diluted with 200 µL of normal RIPA buffer (50 mM Tris-HCl [pH 8.0], 150 mM NaCl, 0.2% SDS, 0.5% sodium deoxycholate, 1% Triton X-100, 1x protease inhibitor cocktail, and 1 mM PMSF), transferred to 3.5 mL ultracentrifuge tubes (Beckman

Coulter), and centrifuged at 100,000 g for 30 minutes at 4°C. 1.5 mL of the supernatant was carefully collected for each sample.

400 µL of streptavidin-coated magnetic beads (Pierce; catalog # 88817) washed twice using 1 ml RIPA buffer were added to each of the post-ultracentrifugation brain lysates. The lysate and the streptavidin bead mixture were left to rotate at 4°C overnight. On the following day, beads were washed twice with 1 mL RIPA buffer, once with 1 mL of 1 M KCl, once with 1 mL of 0.1 M Na_2CO_3, once with 1 mL of 2 M urea in 10 mM Tris-HCl (pH 8.0), and again twice with 1 mL RIPA buffer. The beads were resuspended in 1 mL fresh RIPA buffer. 35 µL of the bead suspension was taken out for western blot, and the rest proceeded to on-bead digestion.

Western blot of biotinylated proteins

Biotinylated proteins were eluted from streptavidin beads by the addition of 20 µL elution buffer (2X Laemmli sample buffer, 20 mM DTT, 2 mM biotin) followed by a 10 min incubation at 95°C. Proteins were resolved by 4%–12% Bis-Tris PAGE gels (Thermo Fisher) and transferred to nitrocellulose membrane (Thermo Fisher). After blocking with 3% bovine serum albumin (BSA) in Tris-buffered saline with 0.1% Tween 20 (TBST; Thermo Fisher) for 1 hour, membrane was incubated with 0.3 mg/mL HRP-conjugated streptavidin for one hour. The Clarity Western ECL blotting substrate (Bio-Rad) and BioSpectrum imaging system (UVP) were used to develop and detect chemiluminescence.

On-bead trypsin digestion of biotinylated proteins

To prepare proteomic samples for mass spectrometry analysis, proteins bound to streptavidin beads were washed twice with 200 µL of 50 mM Tris-HCl buffer (pH 7.5) and twice with 2 M urea/50 mM Tris (pH 7.5) buffer. After washes, the 2 M urea/50 mM Tris (pH 7.5) buffer was removed, and beads were incubated with 80 µL of 2 M urea/50 mM Tris buffer containing 1 mM dithiothreitol (DTT) and 0.4 µg trypsin for 1 hour at 25°C with shaking at 1000 revolutions per minute (rpm). After 1 hour, the supernatant was transferred to a fresh tube. The streptavidin beads were rinsed twice with 60 µL of 2 M urea/50 mM Tris (pH 7.5) buffer and the solution was combined with the on-bead digest supernatant. The eluate was reduced with 4 mM DTT for 30 minutes at 25°C with shaking at 1000 rpm and alkylated with 10 mM iodoacetamide for 45 minutes in the dark at 25°C while shaking at 1000 rpm. An additional 0.5 µg of trypsin was added to the sample and the digestion was completed overnight at 25°C with shaking at 700 rpm. After overnight digestion, the sample was acidified (pH < 3) by adding formic acid (FA) such that the sample contained 1% FA. Samples were desalted on C18 StageTips (3M). Briefly, C18 StageTips were conditioned with 100 µL of 100% MeOH, 100 µL of 50% MeCN/0.1% FA followed by two washes with 100µL of 0.1% FA. Acidified peptides were loaded onto the conditioned StageTips, which were subsequently washed twice with 100 µL of 0.1% FA. Peptides were eluted from StageTips with 50 µL of 50% MeCN/0.1 % FA and dried to completion.

TMT labeling and SCX StageTip fractionation of peptides

8 TMT reagents from a 10-plex reagent kit were used to label desalted peptides (Thermo Fisher) as directed by the manufacturer. Peptides were reconstituted in 100 µL of 50 mM HEPES. Each 0.8 mg vial of TMT reagent was reconstituted in 41 µL of anhydrous acetonitrile and incubated with the corresponding peptide sample for 1 hour at room temperature. Labeling of samples with TMT reagents was completed with the design described in **Fig. 1c**. TMT labeling reactions were quenched with 8 µL of 5% hydroxylamine at room temperature for 15 minutes with shaking,

evaporated to dryness in a vacuum concentrator, and desalted on C18 StageTips as described above. For the TMT 8-plex cassette, 50% of the sample was fractionated into 3 fractions by Strong Cation Exchange (SCX) StageTips while the other 50% of each sample was reserved for LC-MS analysis by a single shot, long gradient. One SCX StageTip was prepared per sample using 3 plugs of SCX material (3M) topped with 2 plugs of C18 material. StageTips were sequentially conditioned with 100 µL of MeOH, 100 µL of 80% MeCN/0.5% acetic acid, 100 µL of 0.5% acetic acid, 100 µL of 0.5% acetic acid/500mM NH_4AcO/20% MeCN, followed by another 100 µL of 0.5% acetic acid. Dried sample was re-suspended in 250 µL of 0.5% acetic acid, loaded onto the StageTips, and washed twice with 100 µL of 0.5% acetic acid. Sample was trans-eluted from C18 material onto the SCX with 100 µL of 80% MeCN/0.5% acetic acid, and consecutively eluted using 3 buffers with increasing pH—pH 5.15 (50mM NH_4AcO/20% MeCN), pH 8.25 (50mM NH_4HCO_3/20% MeCN), and finally pH 10.3 (0.1% NH_4OH, 20% MeCN). Three eluted fractions were re-suspended in 200 µL of 0.5% acetic acid to reduce the MeCN concentration and subsequently desalted on C18 StageTips as described above. Desalted peptides were dried to completion.

Liquid chromatography and mass spectrometry

Desalted, TMT-labeled peptides were resuspended in 9 µL of 3% MeCN, 0.1% FA and analyzed by online nanoflow liquid chromatography tandem mass spectrometry (LC-MS/MS) using a Q Exactive HF-X (Thermo Fisher) coupled on-line to a Proxeon Easy-nLC 1000 (Thermo Fisher). 4 µL of each sample was loaded at 500 nL/min onto a microcapillary column (360 µm outer diameter x 75 µm inner diameter) containing an integrated electrospray emitter tip (10 µm), packed to approximately 24 cm with ReproSil-Pur C18-AQ 1.9 µm beads (Dr. Maisch GmbH) and heated to 50°C. The HPLC solvent A was 3% MeCN, 0.1% FA, and the solvent B was 90% MeCN, 0.1% FA. Peptides were eluted into the mass spectrometer at a flow rate of 200 nL/min. Non-fractionated samples were analyzed using a 260 min LC-MS/MS method with the following gradient profile: (min:%B) 0:2; 1:6; 235:30; 244:60; 245:90; 250:90; 251:50; 260:50 (the last two steps at 500 nL/min flow rate). The SCX fractions were run with 110-minute method, which used the following gradient profile: (min:%B) 0:2; 1:6; 85:30; 94:60; 95:90;100:90; 101:50; 110:50 (the last two steps at 500 nL/min flow rate). The Q Exactive HF-X was operated in the data-dependent mode acquiring HCD MS/MS scans (r = 45,000) after each MS1 scan (r = 60,000) on the top 20 most abundant ions using an MS1 target of 3E6 and an MS2 target of 5E4. The maximum ion time utilized for MS/MS scans was 120 ms (single-shot) and 105 ms (SCX fractions); the HCD normalized collision energy was set to 31; the dynamic exclusion time was set to 20 s, and the peptide match and isotope exclusion functions were enabled. Charge exclusion was enabled for charge states that were unassigned, 1 and > 7.

Mass spectrometry data processing

Collected data were analyzed using the Spectrum Mill software package v6.1 pre-release (Agilent Technologies). Nearby MS scans with the similar precursor m/z were merged if they were within ± 60 s retention time and ± 1.4 m/z tolerance. MS/MS spectra were excluded from searching if they failed the quality filter by not having a sequence tag length 0 or did not have a precursor MH+ in the range of 750 – 4000. All extracted spectra were searched against a UniProt database containing *Drosophila melanogaster* reference proteome sequences. Search parameters included: ESI QEXACTIVE-HCD-v2 scoring parent and fragment mass tolerance of 20 ppm, 30% minimum matched peak intensity, trypsin allow P enzyme specificity with up to four missed cleavages, and calculate reversed database scores enabled. Fixed modifications were carbamidomethylation at

cysteine. TMT labeling was required at lysine, but peptide N termini were allowed to be either labeled or unlabeled. Allowed variable modifications were protein N-terminal acetylation and oxidized methionine. Individual spectra were automatically assigned a confidence score using the Spectrum Mill auto-validation module. Score at the peptide mode was based on target-decoy false discovery rate (FDR) of 1%. Protein polishing auto-validation was then applied using an auto thresholding strategy. Relative abundances of proteins were determined using TMT reporter ion intensity ratios from each MS/MS spectrum and the median ratio was calculated from all MS/MS spectra contributing to a protein subgroup. Proteins identified by 2 or more distinct peptides and ratio counts were considered for the dataset.

Proteomic data cutoff analysis

We used a ratiometric strategy[17] to remove contaminants. Briefly, all detected proteins (2332 with 2 or more unique peptides) were annotated as either true-positives (TPs; proteins with plasma membrane annotation), false-positives (FPs; proteins with either cytosol, mitochondrion, or nucleus annotation but without the membrane annotation), or other annotations according to the subcellular localization annotation in the UniProt database. For each experimental group, we calculated the TMT ratios of proteins in this group compared to one of the controls and sorted proteins in a descending order. For each TMT ratio, a true-positive rate (TPR) and a false positive rate (FPR) were calculated by summing up the number of TPs or FPs with a higher ranking and divided them by the total number of TPs or FPs, respectively. The TPRs and FPRs were used to generate the ROC curves. The cutoff for each experimental-to-control group was determined by finding the TMT ratio where [TPR – FPR] is maximized. Proteins with TMT ratio higher than the cutoff were retained for each experimental group. 459 proteins that passed the cutoffs using both 127N/127C and 126/128N ratios were retained for wild-type, and 537 proteins that passed the cutoffs using both 129N/129C and 128C/130N ratios were retained for *acj6* mutant in **Fig. 1e**. We also tested a more stringent cutoff criterion where we compared each of the experimental group to both controls for each genotype, and only kept proteins that passed the cutoffs in all four possible combinations (**Extended Data Fig. 2**). Gene Ontology analyses were performed on these gene sets using Flymine[63].

Quantitative comparison of wild-type and *acj6* mutant proteomes

For the volcano plots (**Fig. 1g** and **Extended Data Fig. 2c**) comparing differentially enriched proteins in *acj6* mutant PN surface compared to wild-type PN surface, a linear model was fit to account for the variance across replicates for each stage and normalize data by the appropriate negative control samples as previously described[15].

A protein summary was first generated where each TMT condition was calculated as a log ratio to the median intensity of all the channels, enabling all channels to have the same denominator. Following calculation of the $\log_2$ ratio, all samples were normalized by subtracting the median $\log_2$ ratio (median centering). For each protein, a linear model was used to calculate the following ratio and the corresponding *p*-value:

$$\frac{\textit{acj6}\text{ mutant labeling condition (128C, 129N)} \;/\; \textit{acj6}\text{ mutant negative control (129C, 130N)}}{\text{Wildtype labeling condition (126, 127N)} \;/\; \text{Wildtype negative control (127C, 128N)}}$$

Using $\log_2$ transformed TMT ratios, the linear model is as follows:

$$log_2(TMT\ Ratio) \sim MUT * TRT$$

where *MUT* (*acj6* mutant) and *TRT* (treatment) are indicator variables representing *acj6* mutant (*MUT* = 1 for mutant, 0 for wildtype) and labeling condition (*TRT* = 1 for labeled, 0 for negative control) respectively. The above linear model with interaction terms expands to:

$$log_2(TMT\ Ratio) = b_0 + b_1\ MUT + b_2\ TRT + b_3\ MUT * TRT$$

Coefficient b_3 represents the required (log-transformed) ratio between mutant and wildtype conditions taking into account the appropriate negative controls and replicates. A moderated t-test was used to test the null hypothesis of $b_3 = 0$ and calculate a nominal *p*-value for each protein. These nominal *p*-values were then corrected for multiple testing using the Benjamini-Hochberg FDR (BH-FDR) method[64]. **Fig. 1g** and **Extended Data Fig. 2c** show the value of b_3 along the x-axis and the $-\log_2(p\text{-value})$ along the y-axis of the volcano plot.

The linear model along with the associated moderated t-test and BH-FDR correction were implemented using the limma library[65] in R.

We note that the ratio compression effect of the TMT strategy reported previously[66,67] can also compromise the accuracy of our data, and it is not possible for us to estimate the amount of compression without spiked-in standards. However, by using a less complex sample (proximity-labeled rather than whole cell proteomes) and performing offline fractionation prior to MS analysis, we have reduced ratio compression to the best of our ability without sacrificing the number of proteins identified.

Immunocytochemistry

Fly brains were dissected and immunostained according to the previously published protocol[68]. Briefly, fly brains of the desired genotype and developmental stage were dissected in PBS, transferred to a tube with 1 mL of fixation buffer (4% paraformaldehyde in PBS with 0.006% Triton X-100) on ice, and fixed for 20 minutes by nutating at room temperature. After fixation, brains were washed with PBST (0.3% Triton X-100 in PBS) twice, nutated in PBST for 20 minutes twice, and blocked in 5% normal goat serum in PBST for 1 hour (except for conditional tag flies; see below for details). To visualize the antennal lobe glomeruli and PN dendrites, brains were then incubated in rat anti-Ncad (N-Ex #8; 1:40; Developmental Studies Hybridoma Bank) and chicken anti-GFP (1:1000; Aves Labs) diluted in 5% normal goat serum in PBST for two overnights on a 4°C nutator. After primary antibody incubation, brains were washed four time with PBST (two quick washes and two 20-minute washes) and incubated with secondary antibodies conjugated to Alexa Fluor 488 and 647 (1:250 in 5% normal goat serum; Jackson ImmunoResearch). To visualize biotinylated proteins, brains were incubated with Neutravidin (Thermo Fisher) pre-conjugated to Alexa Fluor 647 (Invitrogen). After the antibody incubation(s), brains were washed four times (two quick washes and two 20-minute washes), mounted with SlowFade antifade reagent (Thermo Fisher), and stored at 4°C before imaging.

For the staining of Otk or Dg conditional tag, the above method produced low signal-to-noise FLAG (or V5) signal, so Alexa 488 Tyramide SuperBoost kit (Thermo Fisher) was used to amplify the signal. Briefly, after dissection, fixation, and washing steps, brains were rinsed with PBS twice and incubated with 3% hydrogen peroxide for 1 hour to quench the activity of endogenous peroxidases. Brains were then washed with PBST three times, blocked for 1 hour in 10% goat serum provided by the kit, and incubated with V5 or FLAG antibody diluted in 10% goat serum for two overnights on a 4°C nutator. After four 20-minute washes using PBST, brains were incubated with the poly-HRP-conjugated secondary antibody provided in the kit for two

overnights on a 4°C nutator. Brains were washed four times again with PBST (two quick and two 20-minute washes) and twice with PBS. Afterwards, the brains were incubated with the tyramide solution for 5 minutes at room temperature, and reaction was immediately quenched by three washes using the quenching buffer provided by the kit. Brains were then washed with PBST four times, and NCad staining was performed using standard immunostainng protocol described above.

Image acquisition and processing

Images were obtained with a Zeiss LSM 780 laser-scanning confocal microscope (Carl Zeiss) using a 40x (NA 1.4) oil objective. Z-stacks were acquired at 1-µm intervals at the resolution of 512x512. Brightness and contrast adjustments as well as image cropping were done using ImageJ.

Genetic screen to identify molecules required for adPN dendrite targeting

The adPN screening line was generated by recombining *UAS-dcr2* with *UAS-mCD8-GFP* on the X chromosome and *C15-p65^{AD}* with *VT033006-GAL4^{DBD}* on the third chromosome. Virgin female flies from this screening line were crossed to *UAS-RNAi* or *UAS-cDNA* males, and the progenies were kept at 25°C for 2 days after egg laying and then transferred to 29°C to enhance expression by the GAL4/UAS system. Brains were dissected, immunostained, and imaged as described above.

To quantify adPN dendrite innervation pattern, individual glomeruli were identified using the NCad staining (based on their stereotyped shapes and positions), and then categorical innervation scores (not innervated, weakly innervated, or strongly innervated) were assigned to each of the identified glomeruli. The genotypes were blinded during scoring. Data was analyzed using python packages Pandas and Scipy. For each glomerulus, we calculated the frequency of each type of innervation and plotted the results as stacked bars in **Extended Data Fig. 4**. To quantify if knocking down or overexpressing a gene caused significant dendrite innervation changes, Chi-squared tests were performed on the innervation degree frequencies of a glomerulus of a given genotype compared to control. *p*-values were adjusted for multiple comparisons using Bonferroni correction, and glomeruli whose dendrite innervation were significantly changed (*p*-value < 0.05) were color blue or red in a heatmap shown in **Extended Data Fig. 3b**.

Generation of endogenous conditional tags

Otk or Dg conditional tag flies were generated based on the previously described method[15]. To make the homology-directed repair (HDR) vectors, a ~2000-bp genomic DNA flanking the stop codon was amplified using Q5 hot-start high-fidelity DNA polymerase (New England Biolabs) and inserted into *pCR-Blunt-TOPO* vector (Thermo Fisher). The conditional tag cassette (*FRT-1×V5-6×Stop-loxP-mini-White-loxP-FRT-3×FLAG-6×Stop*) was amplified from the LRP1 plasmid[15] and inserted into the *TOPO genomic sequence plasmid* to replace the stop codon using NEBuilder HiFi DNA assembly master mix (New England Biolabs). CRIPSR guide RNA (gRNA) targeting a locus near the stop codon was designed using the flyCRISPR Target Finder tool[69] and cloned into the *pU6-BbsI-chiRNA* vector (Addgene #45946) by NEBuilder HiFi DNA assembly master mix.

The HDR and the gRNA vectors were co-injected into *vas-Cas9*[70] fly embryos. G_0 flies were crossed to a *white*$^{-}$ balancer and all *white*$^{+}$ progenies were individually balanced. To remove the *loxP*-flanked *miniWhite* cassette, each line was crossed to flies with *hs-Cre*. Fertilized eggs or young larvae were heat shocked twice at 37°C for 1 hour separated a day apart and crossed to a balancer. Their *white*$^{-}$ progenies were individually balanced and verified by sequencing to obtain *gene-FRT-V5-STOP-FRT-FLAG-STOP*.

Quantification of Otk expression in PNs

In ImageJ, individual glomeruli were identified based on the NCad staining, and the average FLAG fluorescence intensities for these glomeruli were measured. The intensities were then normalized to the intensity of the *GH146-FLP*-negative DA4m glomerulus, and the normalized values were plotted in **Extended Data Fig. 6d**. Two-sided t-test of independence was used to compare the Otk expression between wild-type and *acj6* mutant glomeruli, and *p*-values were adjusted using Bonferroni correction.

Generation of UAS flies

To generate UAS flies, we used Q5 hot-start high-fidelity DNA polymerase to amplify the transcripts of each candidate gene from complementary DNA (cDNA) synthesized using the total RNA of w^{1118} fly heads (extracted using MiniPrep kit; Zymo Research). For each candidate gene, we designed more than 2 pairs of PCR primers in the 5' and 3' untranslated regions and inserted all resulting PCR products into *pCR-Blunt-TOPO* vector (Thermo Fisher). The *TOPO-transcript* vectors of the same gene were sequenced and compared to verify that no error was introduced to the coding sequence during reverse transcription. The verified coding sequences were then amplified and assembled into either the *pUAST-attB* vector (*Nep3*) or a modified *pUAST-attB* vector in which a FLAG tag was added at the 3' end (*Dg*, *CG5027*, *DopR*, *Osty*, and *Piezo*). To generate the channel-dead Piezo UAS construct ($Piezo^{M2464A/F2465A}$ or $Piezo^{MF\rightarrow AA}$), we introduced a 6-bp mutation using the Q5 site-directed mutagenesis kit (New England Biolabs). The *pUAST-attB* constructs were inserted into either *attP40* or *attP86Fb* (for *Piezo* constructs) landing sites. G_0 flies were crossed to a $white^-$ balancer, and all $white^+$ progenies were individually balanced and verified by sequencing.

MARCM-based mosaic analysis

hsFlp-based MARCM analyses were performed following the previously published protocol[71]. Each fly contains *GH146-GAL4*, *UAS-mCD8-GFP*, *tubP-GAL80*, *hsFlp*, the desired *FRT*, a mutant allele distal to the *FRT* site (or wild-type for control), and, in rescue experiments, one or two *UAS-candidate gene*. For simplicity, the genotypes for rescue are designated as "$mutant^{-/-}$ + *candidate gene*" in figure labels. The MARCM design (**Extended Data Fig. 5**) ensures that candidate genes under *UAS* control are only expressed in *GH146-GAL4+* mutant clones, uncoupled from their normal regulation (e.g., by Acj6). To generate adPN neuroblast, lPN neuroblast, or DL1 single-cell MARCM clones, flies were heat shocked at 0–24 hours after larvae hatching for 1 hour at 37°C. More than 150 adult brains were dissected for each genotype to get approximately 20 clones.

Quantification of adPN dendrite innervation patterns in MARCM-based mosaic analysis

All images of MARCM clones were given human-unidentifiable names and mixed with all other genotypes before scoring. Individual glomeruli were identified using the NCad staining, and then categorical innervation scores were assigned to identified glomeruli. After scoring, the data were imported into python, and the genotype information was revealed.

To test whether expressing a transgene rescued any dendrite mistargeting phenotypes caused by the loss of Acj6, we first performed Chi-squared test comparing each glomerulus of a given genotype with that glomerulus in wild-type: if the *p*-value was greater than 0.05, we considered it as fully rescued; if the *p*-value was less than 0.05, we further compared the innervation frequencies of this glomerulus of this genotype with that of *acj6* mutant to see if there was significant partial rescue (*p*-value < 0.05 compared to *acj6* mutant). Note that we did not adjust

for multiple comparisons here, because the adjustment would render most mistargeting phenotypes in *acj6* mutant insignificant compared to control and would also fail to detect cases with obvious phenotypic rescue.

Data availability

Mass spectrometry proteomics data will be deposited to MassIVE. Original proteomic data prior to analyses is provided in **Supplementary Table 2**.

Code availability

Custom analysis code will be made available at https://github.com/Qijing-Xie/Acj6.

References

1 Santiago, C. & Bashaw, G. J. Transcription factors and effectors that regulate neuronal morphology. *Development* **141**, 4667-4680, doi:10.1242/dev.110817 (2014).
2 Butler, S. J. & Tear, G. Getting axons onto the right path: the role of transcription factors in axon guidance. *Development* **134**, 439-448, doi:10.1242/dev.02762 (2007).
3 Komiyama, T., Johnson, W. A., Luo, L. & Jefferis, G. S. From lineage to wiring specificity. POU domain transcription factors control precise connections of Drosophila olfactory projection neurons. *Cell* **112**, 157-167, doi:10.1016/s0092-8674(03)00030-8 (2003).
4 Jan, Y. N. & Jan, L. Y. Branching out: mechanisms of dendritic arborization. *Nat Rev Neurosci* **11**, 316-328, doi:10.1038/nrn2836 (2010).
5 Kolodkin, A. L. & Tessier-Lavigne, M. Mechanisms and molecules of neuronal wiring: a primer. *Cold Spring Harb Perspect Biol* **3**, a001727, doi:10.1101/cshperspect.a001727 (2011).
6 Sanes, J. R. & Zipursky, S. L. Synaptic Specificity, Recognition Molecules, and Assembly of Neural Circuits. *Cell* **181**, 1434-1435, doi:10.1016/j.cell.2020.05.046 (2020).
7 Certel, S. J., Clyne, P. J., Carlson, J. R. & Johnson, W. A. Regulation of central neuron synaptic targeting by the Drosophila POU protein, Acj6. *Development* **127**, 2395-2405 (2000).
8 Komiyama, T., Carlson, J. R. & Luo, L. Olfactory receptor neuron axon targeting: intrinsic transcriptional control and hierarchical interactions. *Nat Neurosci* **7**, 819-825, doi:10.1038/nn1284 (2004).
9 Schonemann, M. D. *et al.* POU domain factors in neural development. *Adv Exp Med Biol* **449**, 39-53, doi:10.1007/978-1-4615-4871-3_4 (1998).
10 Jefferis, G. S., Marin, E. C., Stocker, R. F. & Luo, L. Target neuron prespecification in the olfactory map of Drosophila. *Nature* **414**, 204-208, doi:10.1038/35102574 (2001).
11 Marin, E. C., Watts, R. J., Tanaka, N. K., Ito, K. & Luo, L. Developmentally programmed remodeling of the Drosophila olfactory circuit. *Development* **132**, 725-737, doi:10.1242/dev.01614 (2005).

12 Yu, H. H. *et al.* A complete developmental sequence of a Drosophila neuronal lineage as revealed by twin-spot MARCM. *PLoS Biol* **8**, e1000461, doi:10.1371/journal.pbio.1000461 (2010).

13 Lin, S., Kao, C. F., Yu, H. H., Huang, Y. & Lee, T. Lineage analysis of Drosophila lateral antennal lobe neurons reveals notch-dependent binary temporal fate decisions. *PLoS Biol* **10**, e1001425, doi:10.1371/journal.pbio.1001425 (2012).

14 Loh, K. H. *et al.* Proteomic Analysis of Unbounded Cellular Compartments: Synaptic Clefts. *Cell* **166**, 1295-1307 e1221, doi:10.1016/j.cell.2016.07.041 (2016).

15 Li, J. *et al.* Cell-Surface Proteomic Profiling in the Fly Brain Uncovers Wiring Regulators. *Cell* **180**, 373-386 e315, doi:10.1016/j.cell.2019.12.029 (2020).

16 Thompson, A. *et al.* Tandem mass tags: a novel quantification strategy for comparative analysis of complex protein mixtures by MS/MS. *Anal Chem* **75**, 1895-1904, doi:10.1021/ac0262560 (2003).

17 Hung, V. *et al.* Proteomic mapping of the human mitochondrial intermembrane space in live cells via ratiometric APEX tagging. *Mol Cell* **55**, 332-341, doi:10.1016/j.molcel.2014.06.003 (2014).

18 Hong, W. *et al.* Leucine-rich repeat transmembrane proteins instruct discrete dendrite targeting in an olfactory map. *Nat Neurosci* **12**, 1542-1550, doi:10.1038/nn.2442 (2009).

19 Winberg, M. L. *et al.* The transmembrane protein Off-track associates with Plexins and functions downstream of Semaphorin signaling during axon guidance. *Neuron* **32**, 53-62, doi:10.1016/s0896-6273(01)00446-9 (2001).

20 Cafferty, P., Yu, L. & Rao, Y. The receptor tyrosine kinase Off-track is required for layer-specific neuronal connectivity in Drosophila. *Development* **131**, 5287-5295, doi:10.1242/dev.01406 (2004).

21 Shcherbata, H. R. *et al.* Dissecting muscle and neuronal disorders in a Drosophila model of muscular dystrophy. *EMBO J* **26**, 481-493, doi:10.1038/sj.emboj.7601503 (2007).

22 Lee, T. & Luo, L. Mosaic analysis with a repressible cell marker (MARCM) for Drosophila neural development. *Trends Neurosci* **24**, 251-254, doi:10.1016/s0166-2236(00)01791-4 (2001).

23 Kim, S. E., Coste, B., Chadha, A., Cook, B. & Patapoutian, A. The role of Drosophila Piezo in mechanical nociception. *Nature* **483**, 209-212, doi:10.1038/nature10801 (2012).

24 Saotome, K. *et al.* Structure of the mechanically activated ion channel Piezo1. *Nature* **554**, 481-486, doi:10.1038/nature25453 (2018).

25 Peng, Y. R. *et al.* Satb1 Regulates Contactin 5 to Pattern Dendrites of a Mammalian Retinal Ganglion Cell. *Neuron* **95**, 869-883 e866, doi:10.1016/j.neuron.2017.07.019 (2017).

26 Jain, S. *et al.* A Global Temporal Genetic Program for Neural Circuit Formation. *bioRxiv* **09.18.304410** (2020).

27 Morey, M. *et al.* Coordinate control of synaptic-layer specificity and rhodopsins in photoreceptor neurons. *Nature* **456**, 795-799, doi:10.1038/nature07419 (2008).

28 Peng, J. *et al.* Drosophila Fezf coordinates laminar-specific connectivity through cell-intrinsic and cell-extrinsic mechanisms. *Elife* **7**, e33962, doi:10.7554/eLife.33962 (2018).

29 Ghazalpour, A. *et al.* Comparative analysis of proteome and transcriptome variation in mouse. *PLoS Genet* **7**, e1001393, doi:10.1371/journal.pgen.1001393 (2011).

30 Carlyle, B. C. *et al.* A multiregional proteomic survey of the postnatal human brain. *Nat Neurosci* **20**, 1787-1795, doi:10.1038/s41593-017-0011-2 (2017).

31 Wang, D. *et al.* A deep proteome and transcriptome abundance atlas of 29 healthy human tissues. *Mol Syst Biol* **15**, e8503, doi:10.15252/msb.20188503 (2019).

32 Trowbridge, I. S., Collawn, J. F. & Hopkins, C. R. Signal-dependent membrane protein trafficking in the endocytic pathway. *Annu Rev Cell Biol* **9**, 129-161, doi:10.1146/annurev.cb.09.110193.001021 (1993).

33 MacGurn, J. A., Hsu, P. C. & Emr, S. D. Ubiquitin and membrane protein turnover: from cradle to grave. *Annu Rev Biochem* **81**, 231-259, doi:10.1146/annurev-biochem-060210-093619 (2012).

34 Aebersold, R. & Mann, M. Mass-spectrometric exploration of proteome structure and function. *Nature* **537**, 347-355, doi:10.1038/nature19949 (2016).

35 Han, S., Li, J. & Ting, A. Y. Proximity labeling: spatially resolved proteomic mapping for neurobiology. *Curr Opin Neurobiol* **50**, 17-23, doi:10.1016/j.conb.2017.10.015 (2018).

36 Hosp, F. & Mann, M. A Primer on Concepts and Applications of Proteomics in Neuroscience. *Neuron* **96**, 558-571, doi:10.1016/j.neuron.2017.09.025 (2017).

37 Natividad, L. A., Buczynski, M. W., McClatchy, D. B. & Yates, J. R., 3rd. From Synapse to Function: A Perspective on the Role of Neuroproteomics in Elucidating Mechanisms of Drug Addiction. *Proteomes* **6**, E50, doi:10.3390/proteomes6040050 (2018).

38 Coste, B. *et al.* Piezo proteins are pore-forming subunits of mechanically activated channels. *Nature* **483**, 176-181, doi:10.1038/nature10812 (2012).

39 Coste, B. *et al.* Piezo1 and Piezo2 are essential components of distinct mechanically activated cation channels. *Science* **330**, 55-60, doi:10.1126/science.1193270 (2010).

40 Ranade, S. S. *et al.* Piezo2 is the major transducer of mechanical forces for touch sensation in mice. *Nature* **516**, 121-125, doi:10.1038/nature13980 (2014).

41 Woo, S. H. *et al.* Piezo2 is the principal mechanotransduction channel for proprioception. *Nat Neurosci* **18**, 1756-1762, doi:10.1038/nn.4162 (2015).

42 Nonomura, K. *et al.* Piezo2 senses airway stretch and mediates lung inflation-induced apnoea. *Nature* **541**, 176-181, doi:10.1038/nature20793 (2017).

43 Zeng, W. Z. *et al.* PIEZOs mediate neuronal sensing of blood pressure and the baroreceptor reflex. *Science* **362**, 464-467, doi:10.1126/science.aau6324 (2018).

44 Murthy, S. E., Dubin, A. E. & Patapoutian, A. Piezos thrive under pressure: mechanically activated ion channels in health and disease. *Nat Rev Mol Cell Biol* **18**, 771-783, doi:10.1038/nrm.2017.92 (2017).

45 Szczot, M., Nickolls, A. R., Lam, R. M. & Chesler, A. T. The Form and Function of PIEZO2. *Annu Rev Biochem* **90**, 507-534, doi:10.1146/annurev-biochem-081720-023244 (2021).

46 Koser, D. E. *et al.* Mechanosensing is critical for axon growth in the developing brain. *Nat Neurosci* **19**, 1592-1598, doi:10.1038/nn.4394 (2016).

47 Pathak, M. M. *et al.* Stretch-activated ion channel Piezo1 directs lineage choice in human neural stem cells. *Proc Natl Acad Sci U S A* **111**, 16148-16153, doi:10.1073/pnas.1409802111 (2014).

48 Song, Y. *et al.* The Mechanosensitive Ion Channel Piezo Inhibits Axon Regeneration. *Neuron* **102**, 373-389 e376, doi:10.1016/j.neuron.2019.01.050 (2019).

49 Hong, W. & Luo, L. Genetic control of wiring specificity in the fly olfactory system. *Genetics* **196**, 17-29, doi:10.1534/genetics.113.154336 (2014).

50 Lee, T. & Luo, L. Mosaic analysis with a repressible cell marker for studies of gene function in neuronal morphogenesis. *Neuron* **22**, 451-461, doi:10.1016/s0896-6273(00)80701-1 (1999).

51 Golic, K. G. & Lindquist, S. The FLP recombinase of yeast catalyzes site-specific recombination in the Drosophila genome. *Cell* **59**, 499-509, doi:10.1016/0092-8674(89)90033-0 (1989).

52 Xu, T. & Rubin, G. M. Analysis of genetic mosaics in developing and adult Drosophila tissues. *Development* **117**, 1223-1237 (1993).

53 Clyne, P. J. *et al.* The odor specificities of a subset of olfactory receptor neurons are governed by Acj6, a POU-domain transcription factor. *Neuron* **22**, 339-347, doi:10.1016/s0896-6273(00)81094-6 (1999).

54 Tirian, L. & Dickson, B. J. The VT GAL4, LexA, and split-GAL4 driver line collections for targeted expression in the Drosophila nervous system. *bioRxiv*, 198648, doi:10.1101/198648 (2017).

55 Stocker, R. F., Heimbeck, G., Gendre, N. & de Belle, J. S. Neuroblast ablation in Drosophila P[GAL4] lines reveals origins of olfactory interneurons. *J Neurobiol* **32**, 443-456, doi:10.1002/(sici)1097-4695(199705)32:5<443::aid-neu1>3.0.co;2-5 (1997).

56 Xie, Q. *et al.* Transsynaptic Fish-lips signaling prevents misconnections between nonsynaptic partner olfactory neurons. *Proc Natl Acad Sci U S A* **116**, 16068-16073, doi:10.1073/pnas.1905832116 (2019).

57 Larsen, C. W., Hirst, E., Alexandre, C. & Vincent, J. P. Segment boundary formation in Drosophila embryos. *Development* **130**, 5625-5635, doi:10.1242/dev.00867 (2003).

58 Dietzl, G. *et al.* A genome-wide transgenic RNAi library for conditional gene inactivation in Drosophila. *Nature* **448**, 151-156, doi:10.1038/nature05954 (2007).

59 Bai, L. & Carlson, J. R. Distinct functions of acj6 splice forms in odor receptor gene choice. *J Neurosci* **30**, 5028-5036, doi:10.1523/JNEUROSCI.6292-09.2010 (2010).

60 Deng, B. *et al.* Chemoconnectomics: Mapping Chemical Transmission in Drosophila. *Neuron* **101**, 876-893 e874, doi:10.1016/j.neuron.2019.01.045 (2019).

61 Ni, J. Q. *et al.* A genome-scale shRNA resource for transgenic RNAi in Drosophila. *Nat Methods* **8**, 405-407, doi:10.1038/nmeth.1592 (2011).

62 Perkins, L. A. *et al.* The Transgenic RNAi Project at Harvard Medical School: Resources and Validation. *Genetics* **201**, 843-852, doi:10.1534/genetics.115.180208 (2015).

63 Lyne, R. *et al.* FlyMine: an integrated database for Drosophila and Anopheles genomics. *Genome Biol* **8**, R129, doi:10.1186/gb-2007-8-7-r129 (2007).

64 Benjamini, Y. & Hochberg, Y. Controlling the False Discovery Rate - a Practical and Powerful Approach to Multiple Testing. *J R Stat Soc B* **57**, 289-300, doi:DOI 10.1111/j.2517-6161.1995.tb02031.x (1995).

65 Ritchie, M. E. *et al.* limma powers differential expression analyses for RNA-sequencing and microarray studies. *Nucleic Acids Res* **43**, e47, doi:10.1093/nar/gkv007 (2015).

66 Ting, L., Rad, R., Gygi, S. P. & Haas, W. MS3 eliminates ratio distortion in isobaric multiplexed quantitative proteomics. *Nat Methods* **8**, 937-940, doi:10.1038/nmeth.1714 (2011).

67 Savitski, M. M. *et al.* Measuring and managing ratio compression for accurate iTRAQ/TMT quantification. *J Proteome Res* **12**, 3586-3598, doi:10.1021/pr400098r (2013).

68 Wu, J. S. & Luo, L. A protocol for dissecting Drosophila melanogaster brains for live imaging or immunostaining. *Nat Protoc* **1**, 2110-2115, doi:10.1038/nprot.2006.336 (2006).

69 Gratz, S. J. *et al.* Highly specific and efficient CRISPR/Cas9-catalyzed homology-directed repair in Drosophila. *Genetics* **196**, 961-971, doi:10.1534/genetics.113.160713 (2014).

70 Port, F., Chen, H. M., Lee, T. & Bullock, S. L. Optimized CRISPR/Cas tools for efficient germline and somatic genome engineering in Drosophila. *Proc Natl Acad Sci U S A* **111**, E2967-2976, doi:10.1073/pnas.1405500111 (2014).

71 Wu, J. S. & Luo, L. A protocol for mosaic analysis with a repressible cell marker (MARCM) in Drosophila. *Nat Protoc* **1**, 2583-2589, doi:10.1038/nprot.2006.320 (2006).

Acknowledgments

We thank Y. Aso, Y. Rao, V. Ruta, the Bloomington and Vienna *Drosophila* Stock Centers for the fly lines, and Addgene for plasmids. We thank T. Clandinin, J. Kaltschmidt, K. Shen, C. McLaughlin, Z. Li, K. Wong, Y. Ge, J. Ren, D. Pederick, M. Wagner, and members of the Luo lab for technical support and/or insightful advice on this study. We thank Mary Molacavage for administrative assistance. Q.X. was a Bertarelli Fellow. J.L. is a Jane Coffin Childs postdoctoral fellow. L.L. is an investigator of the Howard Hughes Medical Institute. This work was supported by the National Institutes of Health (R01-DC005982 to L.L. and R01-DK121409 to S.A.C. and A.Y.T.) and the Wu Tsai Neurosciences Institute of Stanford University (Neuro-omics grant to A.Y.T., and L.L.).

Author information

Contributions

Q.X., J.L., and L.L. conceived this project. Q.X., J.L., and L.L. designed the proteomic experiments with input from S.H. and A.Y.T. Q.X., J.L., and S.A.S. collected pupae and Q.X., J.L., H.L., C.X., T.L., D.J.L. dissected fly brains for the proteomic experiment. J.L. and S.H. processed proteomic samples. C.X. hand-delivered proteomic samples to the Broad Institute after FedEx messed up the shipment. N.D.U., T.S., D.R.M., and S.A.C. performed post-enrichment sample processing, mass spectrometry, and initial data analysis. Q.X., J.L., and S.H. analyzed proteomic data. Q.X. designed and performed all other experiments with input from J.L. and L.L. and assistance from S.K., R.G., W.W., and D.J.L. Q.X., J.L., and L.L. wrote the manuscript with input from all authors. L.L supervised the project.

Corresponding author

Correspondence to Liqun Luo.

Ethics declarations

Competing interests

The authors declare no competing interests.

Figures

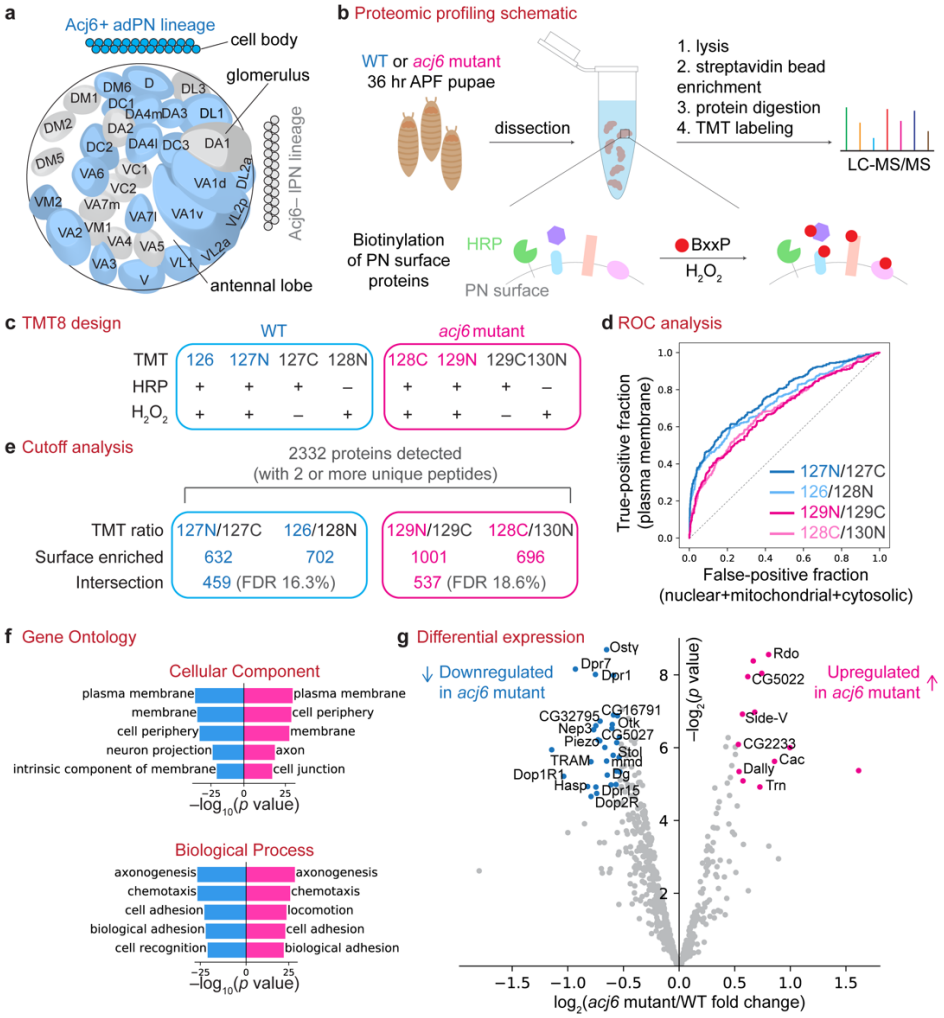

Figure 1 | Identification of Acj6-regulated cell-surface proteins by quantitative proteomic profiling. a, *Drosophila* olfactory projection neurons are derived from either the anterodorsal (adPN) or the lateral (lPN) neuroblast lineage. Acj6 is specifically expressed in adPNs (blue), which target dendrites to a stereotyped subset of glomeruli (blue). **b**, Schematic of PN surface proteomic profiling in developing wild-type and *acj6* mutant brains. Red circle, biotin; APF, after puparium formation. **c**, Design of the 8-plex tandem mass tag (TMT)-based quantitative proteomic experiment. Each genotype comprises two biological replicates (blue or pink) and two negative controls omitting either HRP or H_2O_2 (black). Labels in the TMT row indicate the TMT tag used for each condition. **d**, Receiver operating characteristic (ROC) analysis showing the separation of true positives from false positives in each biological replicate using the experimental-to-control TMT ratio. **e**, Summary of the cutoff analysis. Proteins with TMT ratios greater than the cutoffs in both biological replicates ('Intersection') were retained. FDR, false discovery rate. **f**, Top five Cellular Component and Biological Process Gene Ontology terms for wild-type (blue) and *acj6* mutant (pink) PN surface proteomes. **g**, Volcano plot showing proteins with altered protein levels on *acj6* mutant PN surface compared to wild-type PN surface. Proteins downregulated in *acj6* mutant [$\log_2$(fold change) < –0.53 and p-value < 0.05] are colored in blue. Proteins upregulated in *acj6* mutant [$\log_2$(fold change) > 0.53 and p-value < 0.05] are colored in pink.

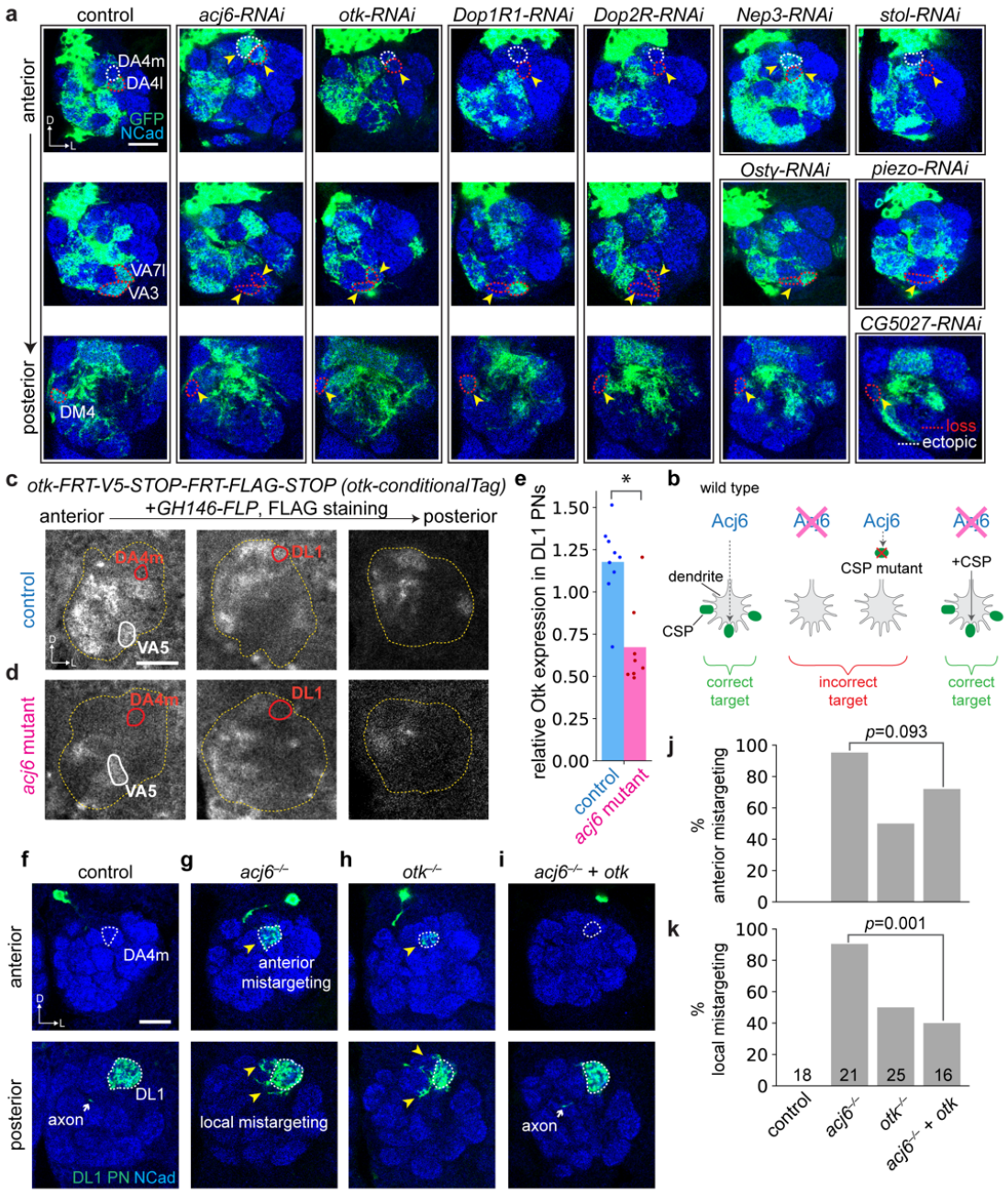

Figure 2 | Acj6-regulated cell-surface proteins instruct PN dendrite targeting. a, Confocal images showing dendrite innervation patterns of *adPN-GAL4*+ PNs (green) in controls and when *acj6* or candidate genes were knocked down by RNAi. Blue, N-cadherin (NCad) staining highlight the glomeruli. Glomeruli with decreased PN dendrite innervation are circled in red while ectopically targeted glomeruli are circled in white. Arrowheads point to the glomeruli exhibiting mistargeting phenotypes. **b**, Criteria of Acj6's cell-surface wiring executors. Loss of either Acj6 or its cell-surface wiring executor would lead to similar dendrite mistargeting. Supplying back the cell-surface wiring executor of Acj6 would rescue *acj6* mutant phenotype. **c**, **d**, Expression of Otk in PNs at 42–48 hr APF in wild-type (**c**) or *acj6* mutant (**d**) brains. Antennal lobe (yellow) and the DA4m, VA5, and DL1 glomeruli are outlined. *GH146-FLP* was used to express FLP in the majority of PNs. **e**, Relative Otk expression in DL1 PNs. See **Extended Data Fig. 6d** for more

detail. **f**, Dendrites of wild-type DL1 single-cell clones innervate exclusively the posterior DL1 glomerulus (n = 18). **g**, *acj6*$^{-/-}$ DL1 single-cell clones mistarget to both nearby glomeruli and a distant anterior glomerulus (n = 21). Yellow arrowhead, mistargeted PN dendrites. **h**, *otk*$^{-/-}$ DL1 single-cell clones phenocopy *acj6*$^{-/-}$ (n = 25). **i**, *acj6*$^{-/-}$ DL1 dendrite mistargeting phenotypes were partially rescued by expressing *otk* (n = 16). **j**, **k**, Quantification of DL1 single-cell clones that mistargeted at a distance (**j**) and locally (**k**). *p*-values of Chi-squared tests are shown on plots. Scale bars, 20 μm. D, dorsal; L, lateral. Arrow, PN axons.

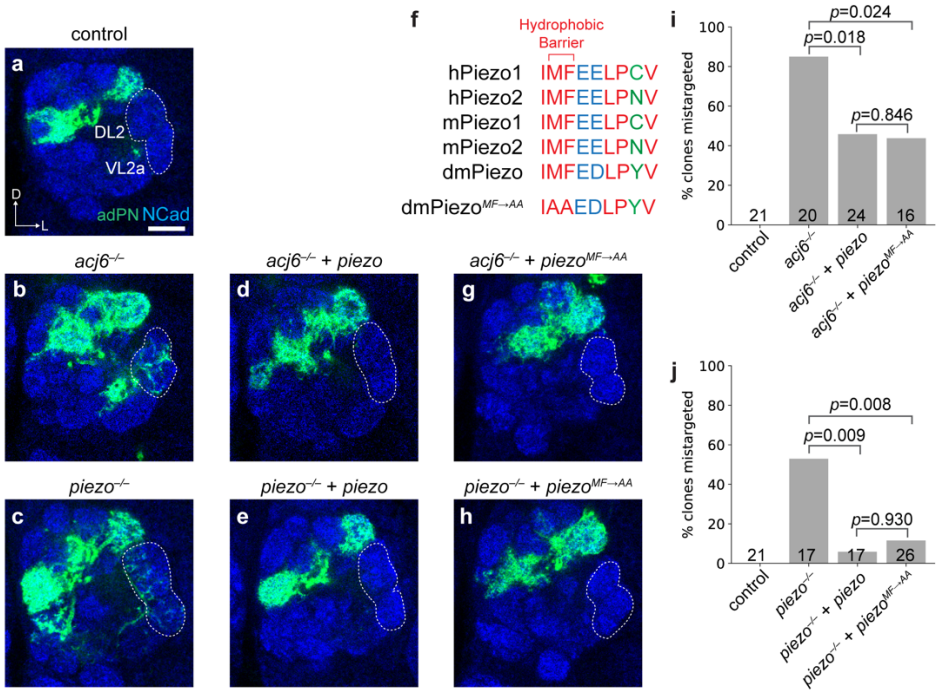

Figure 3 | Piezo is an Acj6 executor for instructing PN dendrite targeting. a–c, Dendrite innervation patterns of wild-type (**a**, n = 21), *acj6*$^{-/-}$ (**b**, n = 20), and *piezo*$^{-/-}$ (**c**, n = 17) adPN neuroblast clones. DL2 and VL2a glomeruli are ectopically innervated in both *acj6* and *piezo* mutants. **d, e,** *acj6*$^{-/-}$ (**d**, n = 24) and *piezo*$^{-/-}$ (**e**, n = 17) mutant phenotypes were rescued by expressing wild-type *piezo*. **f,** Sequence alignment of peptides containing the hydrophobic barrier of human and mouse Piezos 1 and 2 (hPiezo1, 2, mPiezo 1, 2), *Drosophila* wild-type Piezo (dmPiezo) and mutant Piezo predicted to lose its channel activity (dmPiezo$^{MF→AA}$). **g, h,** *acj6*$^{-/-}$ (**g**, n = 16) and *piezo*$^{-/-}$ (**h**, n = 26) mutant phenotypes were rescued by expressing the channel-dead mutant *piezo*$^{MF→AA}$. **i**, **j**, Quantification of adPN dendrites in neuroblast clones that mistargeted to DL2 and VL2 glomeruli in *acj6*$^{-/-}$ (**i**) and *piezo*$^{-/-}$ (**j**) flies. *p*-values of Chi-squared tests are shown. Scale bars, 20 μm. D, dorsal; L, lateral.

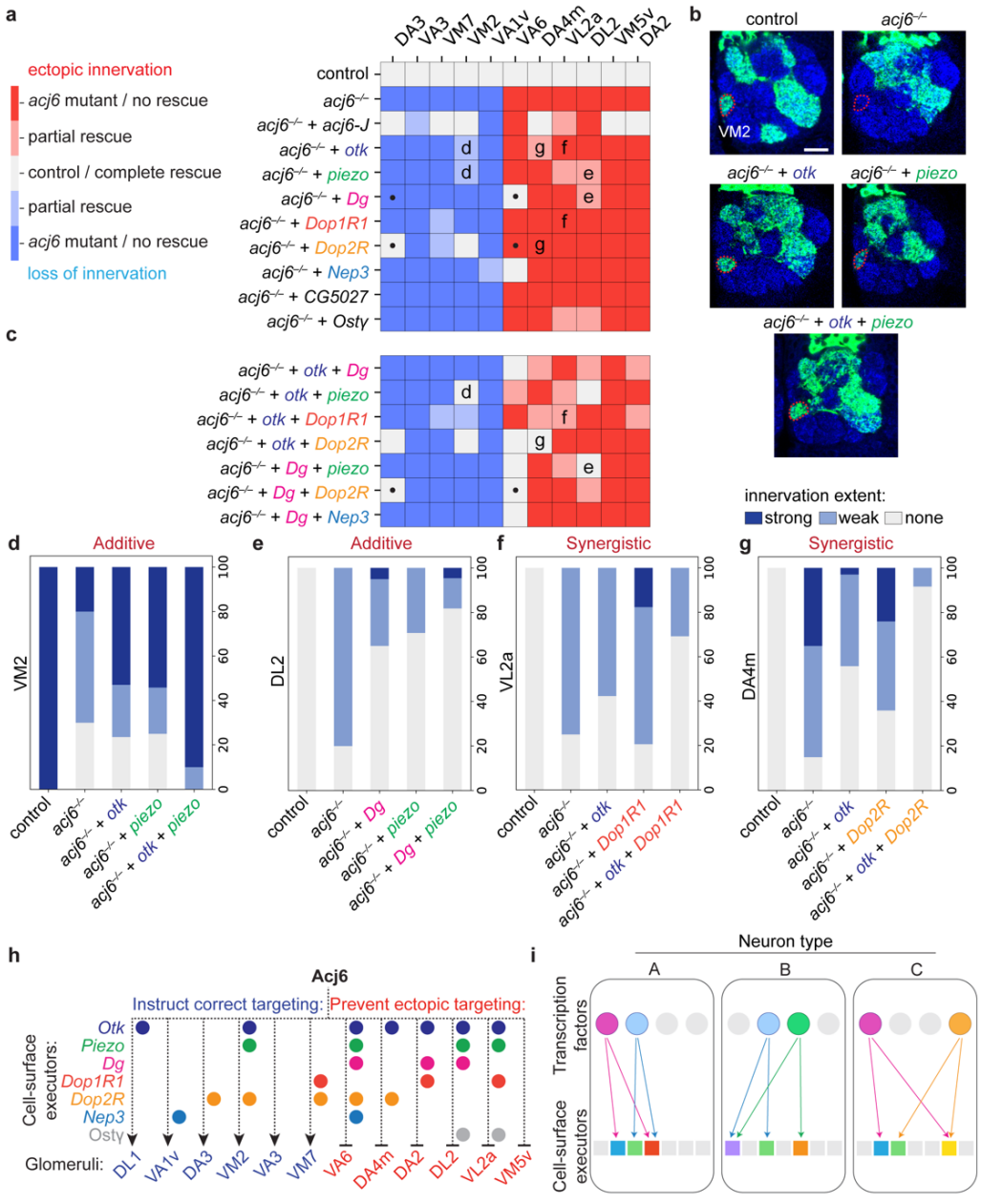

Figure 4 | Acj6 instructs PN wiring through cell-surface combinatorial codes. a, c, Heatmap summarizing changes in the dendrite innervation pattern of adPN neuroblast clones to eleven glomeruli (columns). Dark red (ectopic innervation) and dark blue (loss of innervation) indicate either *acj6* mutant phenotype itself or no rescue of *acj6* mutant phenotype ($p \geq 0.05$ comparing to *acj6* mutant innervation extent, by Chi-squared test here and after). White indicates either the wild-type innervation pattern or complete rescue of *acj6* mutant phenotype ($p \geq 0.05$ comparing to wild-type innervation extent). Light red (ectopic innervation) and light blue (loss of innervation) indicate that the phenotypic rescue was significant ($p < 0.05$ comparing to *acj6* mutant innervation extent) but still different from wild-type ($p < 0.05$ comparing to wild-type innervation extent). Letters within the grids indicate panels where detailed quantifications are shown. Dots highlight an example of between-glomeruli additive interaction ('second type' in the text). **b,** Loss of adPN

dendrite innervation to the VM2 glomerulus in *acj6* mutant was partially rescued by expressing *otk* or *piezo*, and fully rescued by expressing both. Scale bars, 20 μm. **d–g**, Examples of additive (**d**, **e**) and synergistic (**f**, **g**) interactions between Acj6-regulated cell-surface proteins. **h**, Summary of the cell-surface wiring executors of Acj6 for instructing correct targeting or preventing ectopic targeting of adPN dendrites to distinct glomeruli. **i**, Wiring specificity of different neuron types is dictated by cell-surface protein combinatorial codes, which are controlled by combinatorial expression of transcription factors—each transcription factor regulates the expression of multiple cell-surface proteins (divergence), and each cell-surface protein is regulated by multiple transcription factors (convergence).

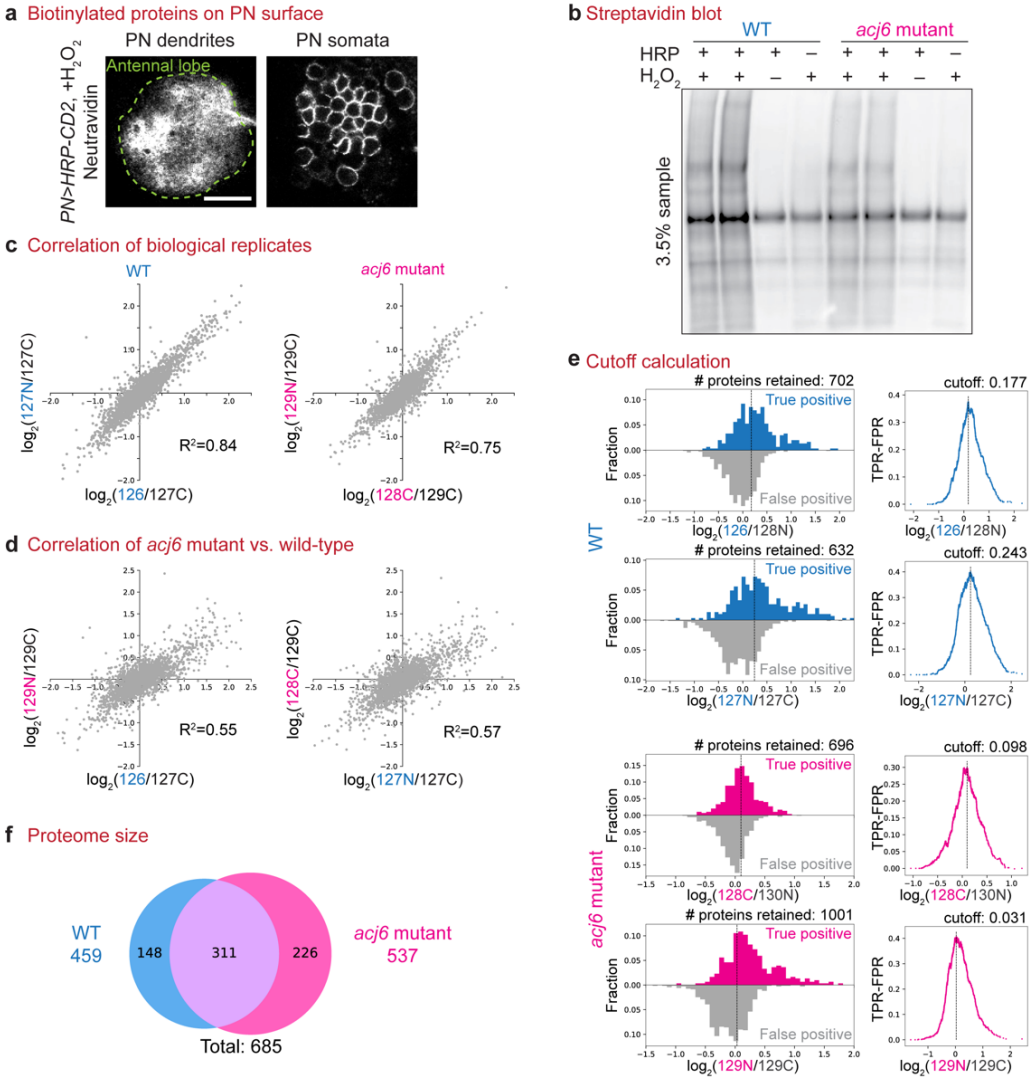

Extended Data Figure 1 | Analysis of PN surface proteomes. a, Neutravidin staining of developing PNs expressing HRP after the cell surface biotinylation reaction. *VT033006-GAL4* is used to drive *UAS-HRP-CD2.* Signals are absent intracellularly in PN somata. **b**, Streptavidin blot of the post-enrichment bead eluate—3.5% from each sample listed in **Fig. 1c**. **c**, Correlation of biological replicates. **d**, Correlation between *acj6* mutant and wild-type samples. **e**, Determination of the TMT ratio cutoffs (dotted vertical lines) for biological replicates in control and *acj6* mutant. **f**, Venn diagram showing the size of and overlap between wild-type and *acj6* mutant PN surface proteomes. TPR, true positive rate; FPR, false positive rate.

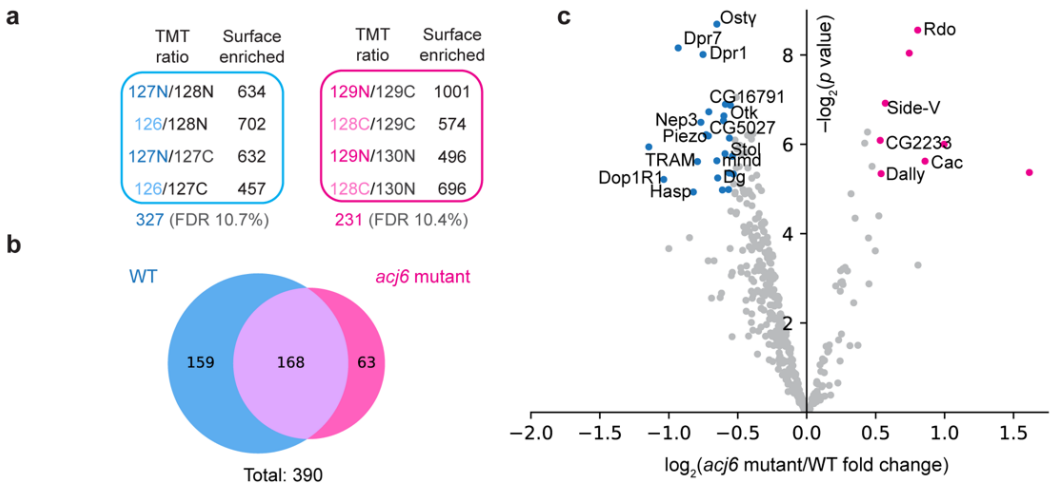

Extended Data Figure 2 | PN surface proteomes using a more stringent cutoff criterion. a, In this more stringent cutoff criterion, a protein must have higher experiment-to-control TMT ratios than the cutoff thresholds in all four possible ratiometric combinations to be included in the final proteome. By this criterion, 327 and 231 proteins were retained in the wild-type (blue) and *acj6* mutant (pink) samples, respectively. **b**, Venn diagram showing the size of and overlap between wild-type and *acj6* mutant PN surface proteomes using this cutoff criterion. **c**, Volcano plot showing proteins with altered expression levels on *acj6* mutant PN surface using this cutoff criterion.

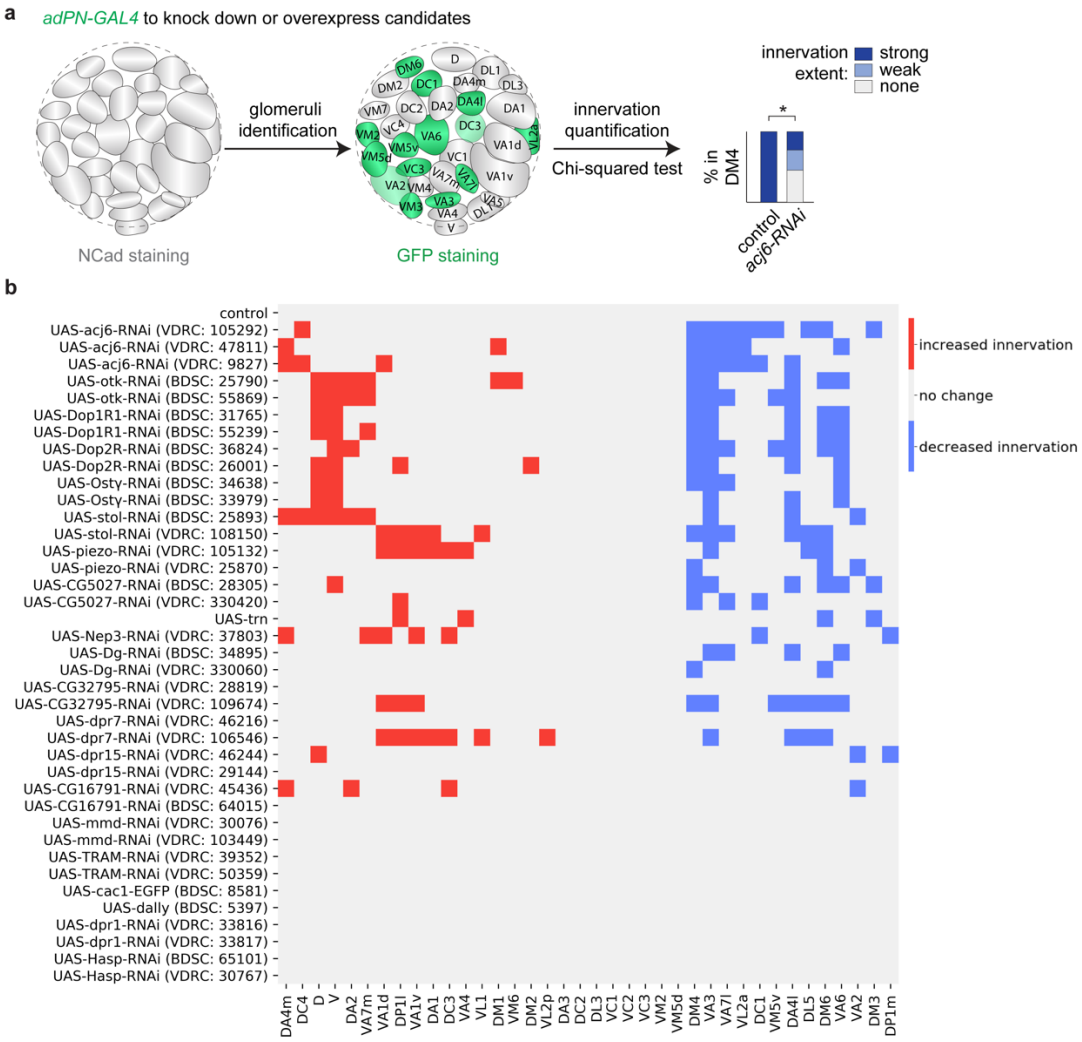

Extended Data Figure 3 | A genetic screen to identify wiring executors of Acj6. a, Schematic of the genetic screen and quantification. An adPN-specific *GAL4* driver line (*C15-p65*^{AD}, *VT033006-GAL4*^{DBD}) was used to knock down candidates down-regulated on *acj6* mutant PN surface or overexpress candidates up-regulated on *acj6* mutant PN surface. Dendrite innervation of each glomerulus was scored into three categories: strong, weak, and none. Scorer was blind to genotypes. **b**, Heatmap summarizing the Chi-squared test results comparing the innervation extent to each glomerulus in each genotype to that in control (data from **Extended Data Fig. 4**). Red, ectopic innervation, $p < 0.05$ (adjusted for multiple comparisons). Blue, loss of innervation, $p < 0.05$ (adjusted for multiple comparisons). Knockdown of some candidates also caused unique dendrite mistargeting patterns not observed in *acj6-RNAi*, suggesting that these molecules also have wiring functions independent of Acj6. Note that RNAi-mediated knockdown experiments could suffer from variation in knockdown efficiency and off-target effects, which likely contributed to some phenotypic inconsistency across different RNAi lines targeting the same candidate.

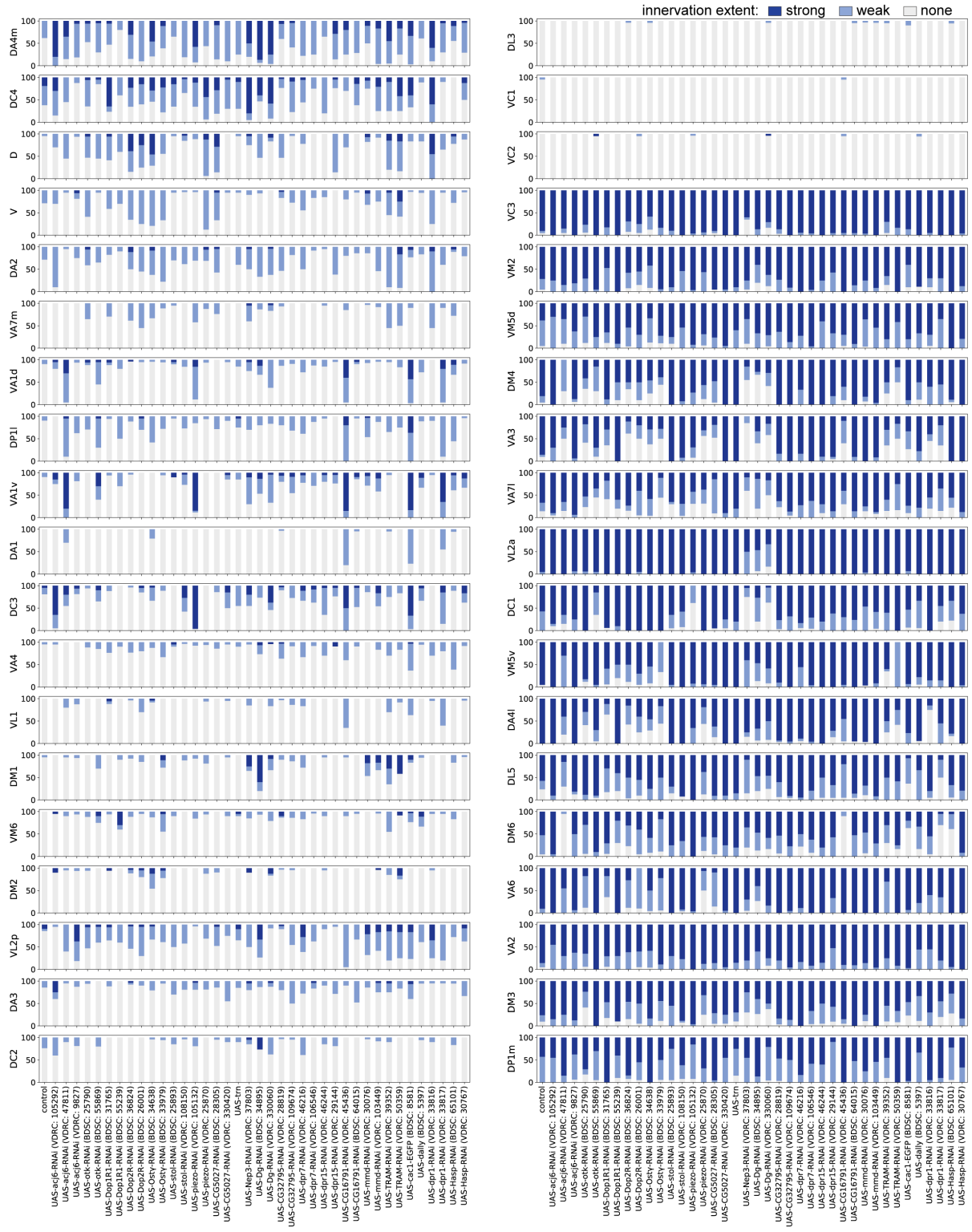

Extended Data Figure 4 | Dendrite innervation patterns of adPNs in the genetic screen. Stacked bar plots summarizing the adPN dendrite innervation pattern to each glomerulus (y-axis) when a given candidate gene was overexpressed or knocked down (x-axis). Categorical scorings (top right) were performed blind to genotypes.

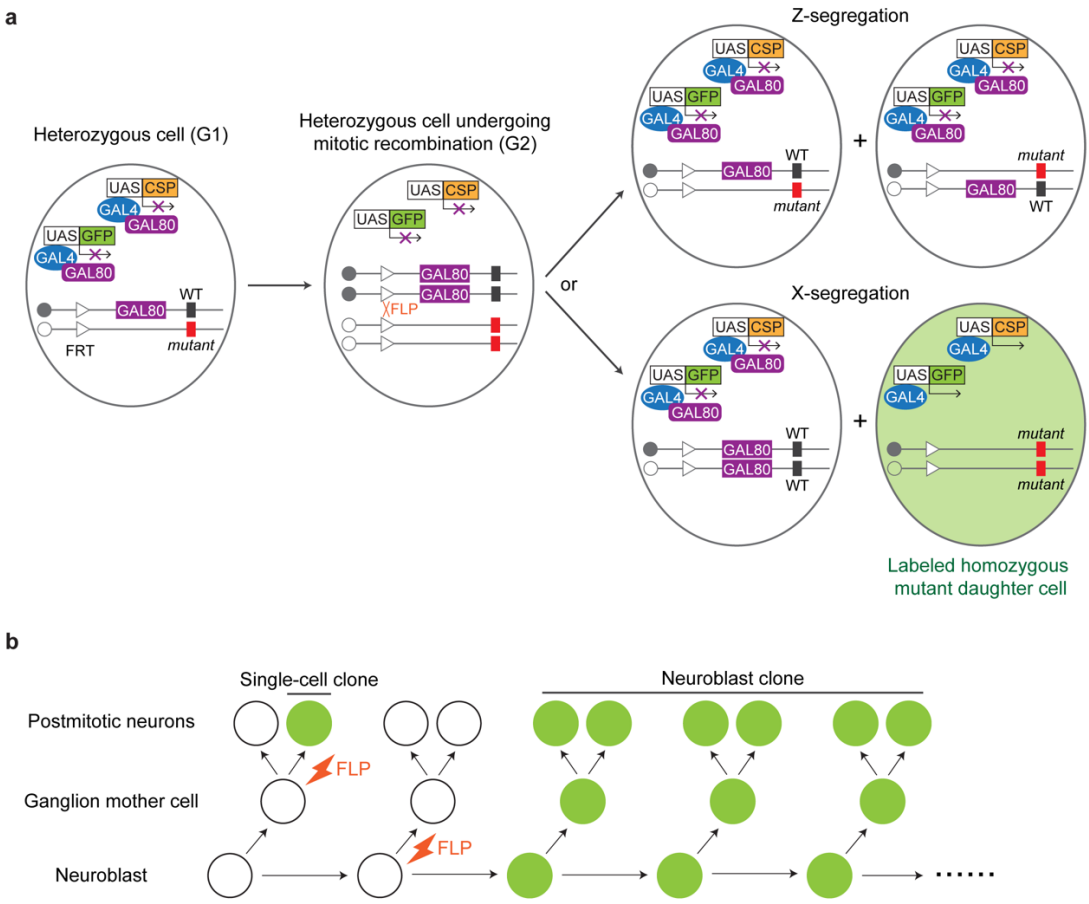

Extended Data Figure 5 | MARCM analysis. a, A mutant (*acj6*, *otk*, or *piezo*) allele is placed on the same chromosome arm in *trans* to a *GAL80* transgene. Heterozygous cells express GAL80, which represses the activity of GAL4 and are thus unlabeled by GFP. After FLP-mediated mitotic recombination followed by X-segregation (bottom row), one of the daughter cells will be homozygous for the mutant and will lose *GAL80*. Those homozygous mutant cells will be labeled with GFP and can also express one or two candidate cell surface proteins (CSP) for the rescue assay. Mitotic recombination followed by Z-segregation (top row) does not generate daughter cells with altered genotype or transgene expression, and are thus not detected. **b**, Illustration of cell division patterns in a neuroblast lineage. MARCM can be used to generate GFP-labeled PN single-cell or neuroblast clones. In this study, all clones were induced by heat shock applied in newly hatched larvae (0–24 hr after larval hatching), so our analyses are restricted to the larval-born adPNs and lPNs (neuroblast clones) and DL1 single-cell clones[10].

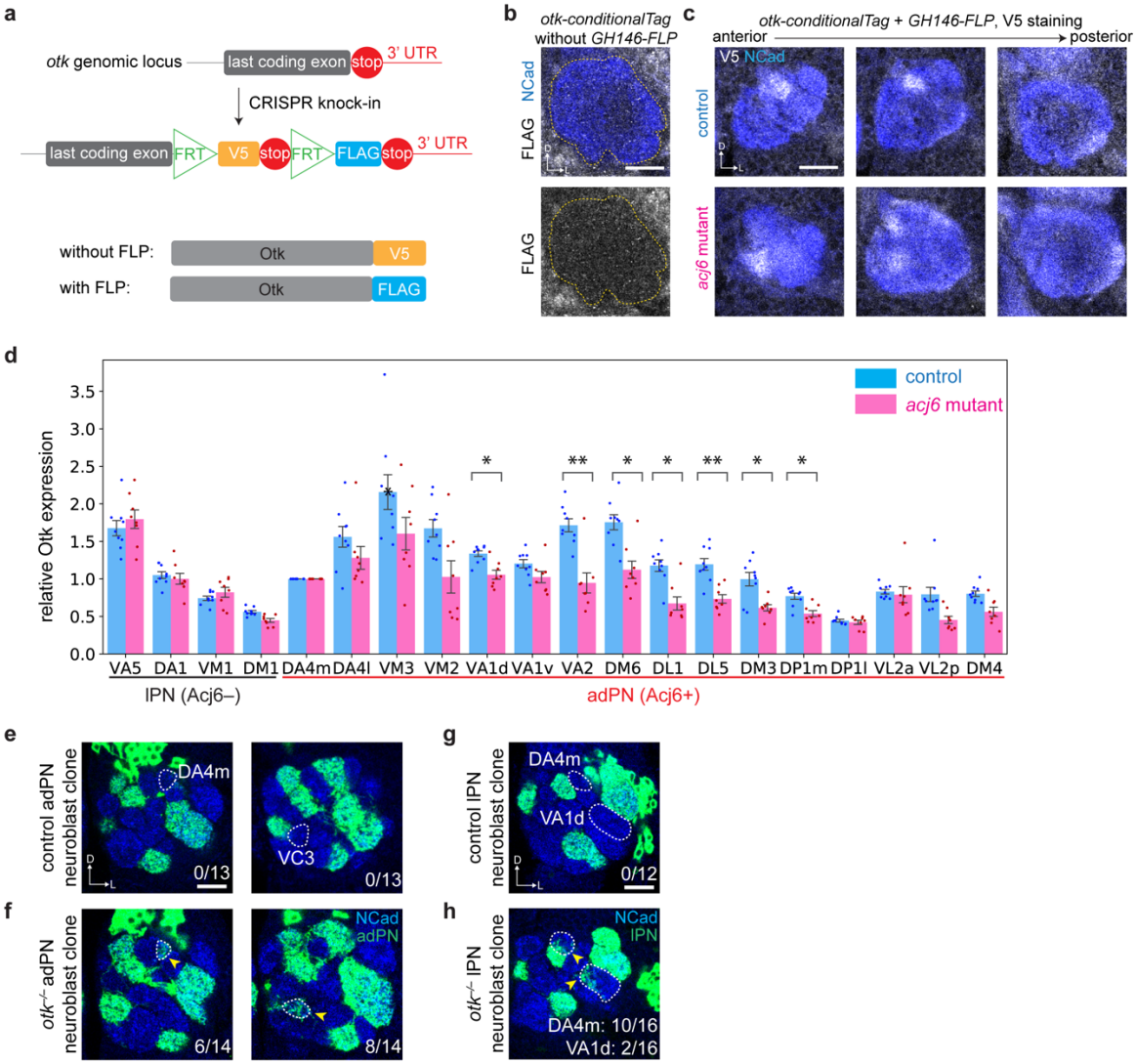

Extended Data Figure 6 | Otk expression pattern and other *otk* mutant phenotypes. a, Schematic of endogenous conditional tagging of Otk to reveal its cell-type-specific protein expression pattern. **b**, *otk-conditionalTag* has minimal FLAG background in the antennal lobe (circled in yellow) without FLP expression. **c**, V5 staining showing the expression of Otk in the antennal lobe contributed by *GH146-FLP*-negative cell types, which potentially include ORN axons, local interneurons, glia, and a small fraction of PNs that do not express *GH146-FLP*. **d**, Quantification of Otk expression in developing PNs of wild-type (n=9) and *acj6*-mutant (n=8) animals. Fluorescence intensities were normalized to the DA4m glomerulus (*GH146-FLP* negative) in each antennal lobe. Mean ± s.e.m. *: $p < 0.05$; **: $p < 0.01$ (two-tailed t-test; *p*-values were adjusted for multiple comparisons). Note that the fluorescence intensity is always lower in deeper (more posterior) sections due to tissue scattering, so the absolute intensity cannot be compared across different PN types. **e**, **f**, DA4m and VC3 glomeruli were ectopically innervated by *otk*$^{-/-}$ adPN neuroblast clones (**f**) compared to wild-type (**e**). **g**, **h**, DA4m and VA1d glomeruli were ectopically innervated by *otk*$^{-/-}$ lateral neuroblast clones (**h**) compared to wild-type (**g**). The number of clones with mistargeting phenotype over the total number of clones examined is noted at the bottom right corner of each panel. Scale bars, 20 μm. D, dorsal; L, lateral.

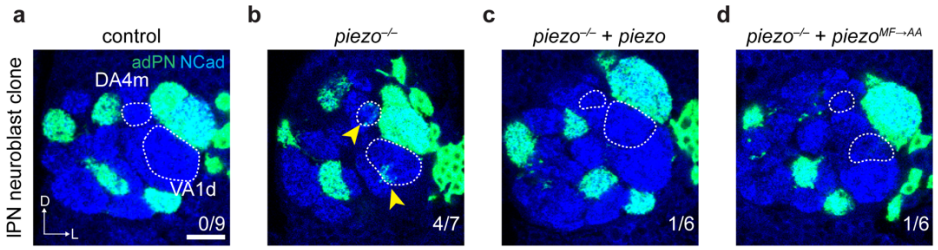

Extended Data Figure 7 | *piezo* mutant phenotypes in lPN neuroblast clones. Dendrite innervation patterns of control (**a**), *piezo*$^{-/-}$ (**b**), *piezo*$^{-/-}$, *UAS-piezo* (**c**), and *piezo*$^{-/-}$, *UAS-piezo*$^{MF\rightarrow AA}$ (**d**) lPN neuroblast clones. The number of clones with mistargeting phenotype over the total number of clones examined is noted at the bottom right corner of each panel. Scale bars, 20 μm. D, dorsal; L, lateral.

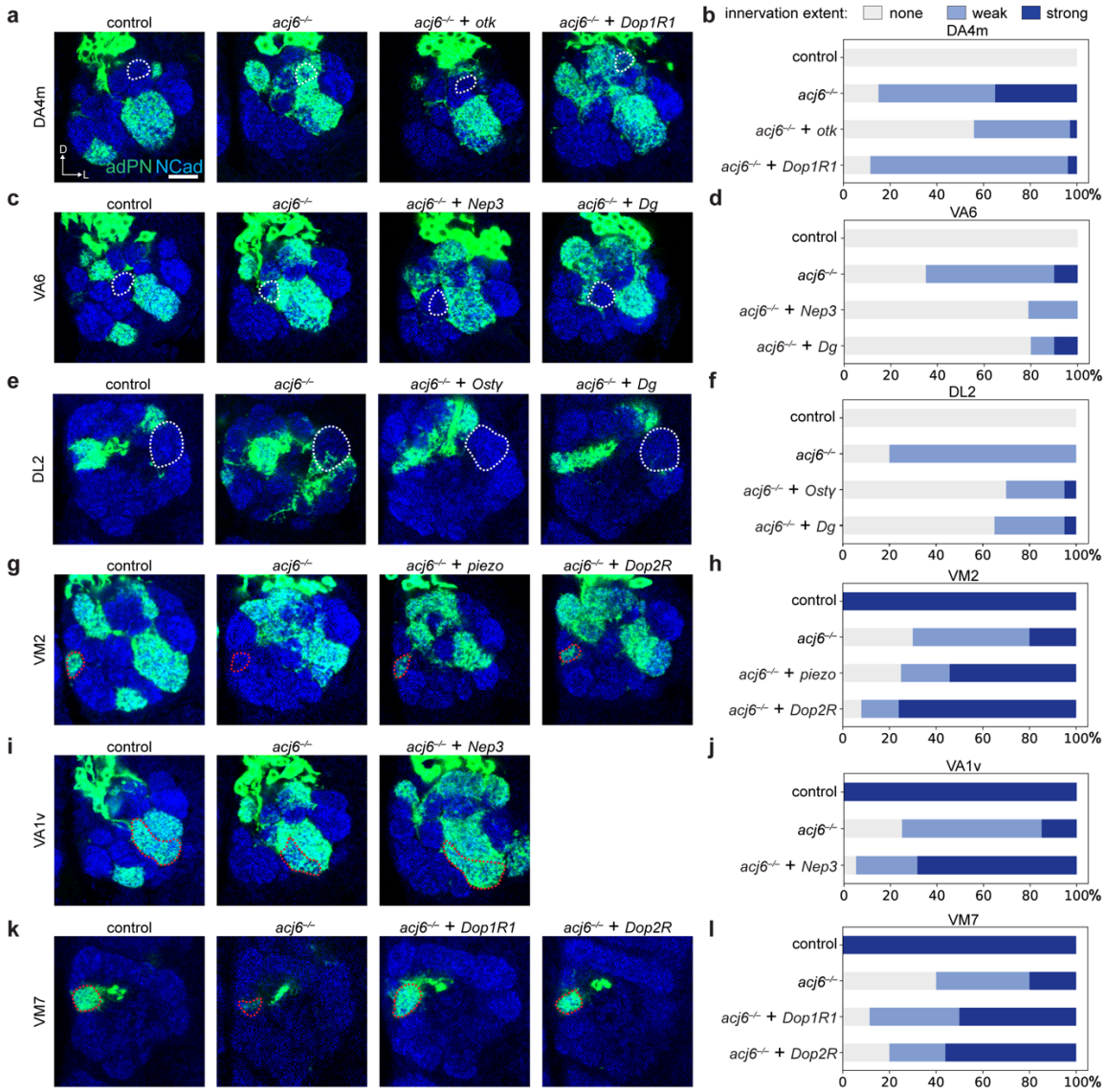

Extended Data Figure 8 | *acj6* mutant phenotypes rescued by individual cell-surface executors. a, **b**, Ectopic targeting of adPN dendrites in adPN neuroblast clones (adPN dendrites hereafter) to the DA4m glomerulus in *acj6* mutant was partially rescued by expressing *otk* or *Dop1R1*. **c**, **d**, Ectopic targeting of adPN dendrites to the VA6 glomerulus in *acj6* mutant was partially rescued by expressing *Nep3* or *Dg*. **e**, **f**, Ectopic targeting of adPN dendrites to the DL2 glomerulus in *acj6* mutant was partially rescued by expressing *Osty* or *Dg*. **g**, **h**, Loss of adPN dendrite innervation in the VM2 glomerulus in *acj6* mutant was partially rescued by expressing *piezo* or *Dop2R*. **i**, **j**, Loss of adPN dendrite innervation in the VA1v glomerulus in *acj6* mutant was partially rescued by expressing *Nep3*. **k**, **l**, Loss of adPN dendrite innervation in the VM7 glomerulus in *acj6* mutant was partially rescued by expressing *Dop1R1* or *Dop2R*. Bar graphs show fractions of clones belonging to three categories of innervation extent: strong, weak, and none. Scale bars, 20 μm. D, dorsal; L, lateral.

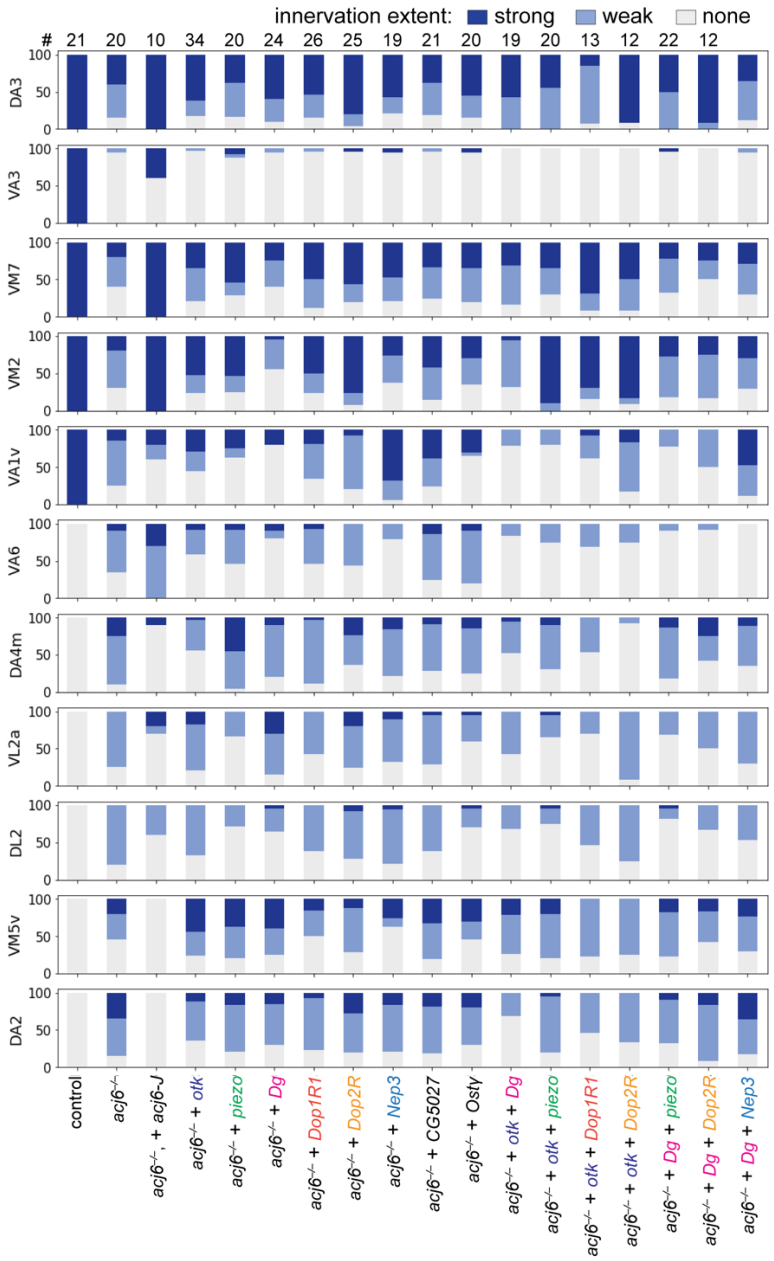

Extended Data Figure 9 | Dendrite innervation patterns of adPNs in the epistasis experiments. Stacked bar plots summarizing dendrite innervation pattern of adPN neuroblast clones to each glomerulus in each genotype. Confocal stacks of different genotypes were scrambled and blinded during scoring. Total number of adPN neuroblast clones examined for each genotype is labeled on top. Note that occasionally expression of an Acj6-regulated cell-surface protein rescued *acj6* mutant phenotypes better than expression of *acj6* itself. Because *acj6* exhibits alternative splicing to produce 13 isoforms[7,59], one possible explanation is that different PN types express different *acj6* isoforms to regulate the expression of different cell-surface executors, so expressing a specific one (isoform J in our case) may not be able to rescue all *acj6* mutant phenotypes. Another possible explanation is the delayed onset of MARCM-based expression due to GAL80 perdurance and the earlier action of a transcription factor compared to its downstream cell-surface executors.

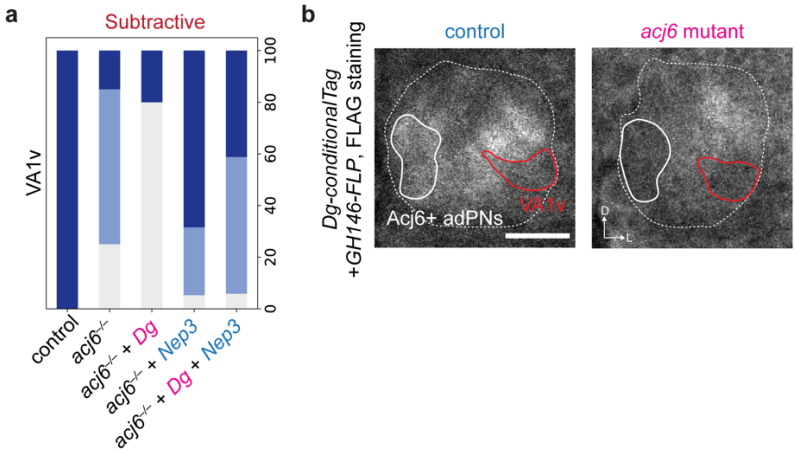

Extended Data Figure 10 | Subtractive interaction between cell-surface executors of Acj6. a, Dg expression exacerbated the loss of VA1v innervation phenotype in *acj6* mutant. Co-expressing Dg with Nep3, whose expression rescued loss of innervation to the VA1v glomerulus, diminished the rescue effect of Nep3. **b**, Dg conditional tag staining indicates that Dg is not expressed in VA1v PNs (red outline) at 42–48 hr APF. Therefore, the worsened phenotype seen in (**a**) is likely caused by mis-expression of Dg. Many medial glomeruli innervated by adPN dendrites (white outline) have lower Dg level in *acj6* mutant animals. Scale bars, 20 μm. D, dorsal; L, lateral.